

First-Principles Investigation of X_2NiH_6 ($X = Ca, Sr, Ba$) Hydrides for Hydrogen Storage Applications

K. Aafi ¹, Z. El Fatouaki ¹, A. Jabar ^{2,3}, A. Tahiri ^{1,4,5}, M. Idiri ¹

¹ LPMC, Department of Physics, Faculty of Sciences, Ben M'Sik, Hassan II University of Casablanca, Casablanca, 7955, Morocco

² LMHEP, Faculty of Sciences Aïn Chock, Hassan II University of Casablanca, B.P. 5366 Casablanca, Morocco

³ LPHE-MS, Science Faculty, Mohammed V University in Rabat, Rabat, Morocco

⁴ Laboratory of Innovation in Sciences, Technologies, and Modeling (ISTM), Department of Physics, Faculty of Sciences, Chouaib Doukkali University, 24000 El Jadida, Morocco

⁵ Laboratory of Advanced Materials and Applications (LM2A), Faculty of Sciences, Sidi Mohamed Ben Abdellah University, B.P.1796 Fez-Atlas, Morocco

***Corresponding author:**

Abstract

First-principles DFT calculations were conducted to analyse the physic properties of hydrides Ca_2NiH_6 , Sr_2NiH_6 and Ba_2NiH_6 . Thermodynamic analysis claimed that, as fundamental principles would predict, all three compounds exhibit rising entropy and heat capacity with increasing temperature. Enthalpy and Gibbs free energy calculations indicate that materials are thermodynamically stable with negative free energies of progressively more negative values at elevated temperatures. Additionally, entropy changes associated with hydrogen adsorption and desorption were found to have a significant part to play in the reversibility in addition to the kinetics of the hydrogen storage process. Optical property calculations including the energy-dependent dielectric function and refractive index indicate that Ba_2NiH_6 exhibits a high refractive index at low energies. These findings are significant in understanding the optical properties and hydrogen storage potential of these compounds and hence for designing efficient energy storage devices. The three nickel hydrides, Ca_2NiH_6 , Sr_2NiH_6 and Ba_2NiH_6 , have been characterized in terms of their mechanical properties. Sr_2NiH_6 with maximum bulk modulus and axial stiffness are very incompressible and have moderate malleability. Ca_2NiH_6 possesses the highest Young's and shear moduli which indicate high resistance to deformation, whereas Ba_2NiH_6 is most compressible and highly deformable. These outcomes are valuable sources of information regarding the structural integrity and mechanical response of these materials at operating conditions, e.g., cyclic pressure and temperature, particularly relevant to their use for hydrogen storage. The results present the calculated formation energies

and hydrogen storage capacities for the investigated hydrides, and these are found to reflect that Ca_2NiH_6 is the most thermodynamically stable among the considered compounds. The hydrides play vital roles in hydrogen storage technology, and the calculated storage capacity values of 4.005 wt%, 2.548 wt%, and 1.750 wt% for Ca_2NiH_6 , Sr_2NiH_6 , and Ba_2NiH_6 are additional evidences to their importance. As a result of its improved hydrogen storage capacity, Ca_2NiH_6 is a useful compound in future hydrogen storage technology.

Keywords: DFT; Hydrogen storage; Electronic properties; Thermodynamic properties; Mechanical properties; Optic properties.

1. Introduction

Energy is a driver of development worldwide, and it has become necessary due to an increasing population and industrialization [1,2]. Presently, energy supplies about 85% from fossil fuels such as coal, oil, and natural gas; this source remains dominant even with the severe environmental impacts it creates [2,3]. The transport sector alone uses about 45% of world energy, which highly contributes to greenhouse gas emissions and health hazards due to both gases and particles emitted into the atmosphere [1]. A transition towards clean and renewable sources of energy is now seen as a priority in achieving growth while reducing carbon emissions [2,4].

Hydrogen is being viewed as a promising carbon-free energy carrier since it is abundant, has high energy density, and is environmentally compatible [1,5-7]. Green hydrogen, obtained by renewable-powered electrolysis, offers a promising pathway toward the decarbonization of energy-intensive transport, power generation, and industry sectors [4]. However, the efficiency and safety of hydrogen storage remain a big challenge [6-8]. Among various storage approaches like compressed gas, liquid hydrogen, and solid-state materials, metal hydrides are under the spotlight due to their high volumetric capacity for storage, reversible hydrogen absorption-desorption properties, and good safety characteristics [8,9].

Hydrogen has become a versatile energy carrier for all sorts of energy demands, ranging from its use as fuel for combined heat and power plants, households, energy storage systems, to hydrogen fuel cell vehicles [10]. However, achieving high-capacity hydrogen storage presents a big challenge. Among the available storage technologies, metal hydride-based systems exhibit high hydrogen storage capacities with substantial promise for future energy applications to meet the increasing global energy demands [3].

Hydrogen energy storage compounds should satisfy a number of critical requirements for practical viability, including high gravimetric and volumetric capacities, reversibility, hydrogen release under ambient conditions, and favorable reaction kinetics [11]. In relation to that, solid-state hydrogen storage has gained considerable research interest, since it opens up much safer and more efficient pathways for hydrogen storage compared to its gaseous or liquid forms [6]. Because solid-state hydrogen storage has higher volumetric hydrogen density and wider practical applicability than either of the other two forms, namely, compressed or liquid hydrogen storage, it has emerged as a highly promising alternative for efficient and safe hydrogen storage technologies [12]. In this regard, metal hydrides are among the most studied materials because of their ability to absorb and desorb hydrogen reversibly under relatively mild conditions [6]. In addressing the general challenge of resource depletion, there is a need to formulate governmental policies capable of balancing the energy requirements of society with the adequate protection of natural resources [13]. This is through the enactment of regulations aimed at conserving resources, investment in renewable energy sources like solar and wind, and promotion of innovative technologies and infrastructures so as to achieve sustainability in human development [13].

Research indicates that $K_2LiGaHH_6$ has a gravimetric hydrogen storage capacity of 3.22% weight percent. Rb_2LiGaH_6 (2.16 wt%), K_2LiInH_6 (2.60 wt%), K_2LiTlH_6 (1.88 wt%), and Rb_2LiInH_6 (1.86 wt%) follow in order. Q_2LiMH_6 is one of the best-capacity and most stable possible future hydrogen storage compounds [14]. By Density Functional Theory (DFT) calculations, the current work examines the mechanical, electrical, optical, and hydrogen storage properties of the X_2MgTiH_6 perovskites ($X = Li, Na, \text{ and } K$) with Li_2MgTiH_6 , Na_2MgTiH_6 , and K_2MgTiH_6 possessing corresponding hydrogen capacities of 6.16 weight percent, 4.64% weight percent, and 3.72% weight percent [15]. Density functional theory calculations reveal perovskite hydrides $KNaX_2H_6$ to be stable for the purpose of hydrogen storage based on their thermodynamic, dynamic, and cubic structural stability. $KNaMg_2H_6$, unlike $KNaCa_2H_6$, presents a high gravimetric hydrogen storage capacity of 5.19% [16]. We have studied some properties of the molecules $NaXH_3$ and KXH_3 using the Cambridge Serial Total Energy Package (CASTEP) where X is Tc, Ru, and Rh. For $NaTcH_3$, $NaRuH_3$, $NaRhH_3$, $KTcH_3$, $KRuH_3$, and $KRhH_3$, the corresponding gravimetric hydrogen storage capacities are 2.44%, 2.38%, 2.35%, 2.16%, 2.11%, and 2.08% weight percent [17]. This study uses first-principles calculations to analyze the $K_2BA_{1-x}Ga_xH_6$ ($B=Li, Na; x = 0, 0.25, 0.5, 0.75, 1$) double perovskite hydrides. On a hydrogen storage potential investigation, K_2LiAlH_6 has the

highest gravimetric hydrogen capacity (5.12 wt%), but the increased atomic mass of Ga causes its storage capacity to decrease with the increasing content [18]. The study estimated that Sr_2TiH_5 , Ca_2TiH_5 , and Mg_2TiH_5 have a hydrogen storage capacity of 2.21%, 3.78%, and 4.97% weight percent, respectively, which can only meet the US-DOE requirement in 2020, and X_2TiH_5 can also store hydrogen [19]. Complex metal hydrides have been attracting increasing attention in recent years, which to a large extent has been spurred by first-principles computational research aimed at predicting the optimal materials for hydrogen storage. Theoretical approaches play a crucial role in the high-throughput screening and prediction of structural, thermodynamic, and electronic properties of new compounds prior to their experimental synthesis. Several materials have been explored in this context, among which alanates are found to exhibit excellent thermodynamic properties, e.g., M_2LiAlH_6 (M = Na, K) and X_2AlH_7 (X = Ca, Sr and Ba) [20].

Hydrogen is chemically stored in the solid state, which can achieve storage density that is far beyond what the conventional method can offer [21]. High and safe, efficiently reversible hydrogen storages demand materials with appropriate absorption/desorption temperature, favorable thermal properties, high storage capacity, and structural features that allow strong interaction of hydrogen [22, 23]. In this regard, stability, appropriate reaction kinetics, mechanical integrity, and effective hydrogen release under realistic conditions are also very important [24]. The ultimate objective is the development of materials capable of working at moderate pressures and temperatures, typically in the range 298–473 K and 1–10 bar, for the delivery of hydrogen applications that are practical and safe [25].

These findings indicate the potential of Ca, Sr, and Ba hydrides as solid-state hydrogen storage media. Due to their high storage capacity and mechanical stability, these media are promising candidates for use in fuel cells and portable energy devices. However, they are water-sensitive and have relatively low hydrogen absorption and desorption rates, suggesting that further research is needed for practical applications [26].

Future research should strive to investigate the influence of various strain types and defect amounts in a bid to further enhance the performance of the material. Experimental confirmation of calculated predictions will also be required to verify theoretical findings and further improve existing models for an improved approximation [27].

Among the several alternatives proposed, solid-state hydrogen storage by means of metal hydrides has gained considerable attention, and among these, there are some alkaline-earth hydrides like Ca_2NiH_6 , Sr_2NiH_6 and Ba_2NiH_6 that show particularly interesting properties.

This work will theoretically study structural, electronic, phononic, thermodynamic, and mechanical properties, including the hydrogen adsorption and desorption mechanisms using the Density Functional Theory. The study of thermodynamic stability, vibrational behavior, and mechanical durability will give insight into its storage efficiency. Optical properties are discussed in view of potential applications in optoelectronic and photovoltaic devices. A theoretical framework is set out for the identification of promising candidates for hydrogen storage and for guiding the future experimental and technological research.

2. Computational method

First-principles calculations were carried out by employing the CASTEP computational package within the framework of DFT. In this method, exchange-correlation interactions are approximated by the generalized gradient approximation [28] through the Perdew-Burke-Ernzerhof functional [29], and for core-valence electron interactions, the projector augmented-wave method is used. The calculations were performed utilizing a plane-wave basis with an energy cutoff of 500 eV and sampling of the Brillouin zone with a $4 \times 4 \times 4$ Monkhorst-Pack k-point mesh in order to attain convergence in the total energy and electrical properties. Structural optimizations were performed with convergence criteria set as: total energy of 5×10^{-6} eV/atom, maximum force of 0.01 eV/Å, maximum displacement of 5×10^{-4} Å, and maximum stress of 0.02 GPa. All calculations were performed at standard conditions of 0 K and 0 GPa. Vanderbilt ultrasoft pseudopotentials (USPP), offering an efficient and accurate representation of the ion–electron potential, were employed to accurately describe electron-ion interactions [30]. The Broyden-Fletcher-Goldfarb-Shanno (BFGS) algorithm was employed for optimization using ultrafine convergence parameters for computational efficiency [31]. The electronic configurations of the constituting atoms are provided below: Ba ($1s^1 2s^2 2p^6 3s^2 3p^6 3d^{10} 4s^2 4p^6 4d^{10} 5s^2 5p^6 6s^2$), Ca ($1s^1 2s^2 2p^6 3s^2 3p^6 4s^2$), Sr ($1s^1 2s^2 2p^6 3s^2 3p^6 3d^{10} 4s^2 5s^2$), Ni ($1s^1 2s^2 2p^6 3s^2 3p^6 3d^8 4s^2$) and H ($1s^1$)

3. Results and discussions

3.1. Properties of structure and hydrogen storage

Figure 1 Indicates the general structural formula for the crystal structures of complex hydrides X_2NiH_6 (X= Ca, Sr and Ba). The compound crystallizes in a space group of perfect cubic symmetry Fm-3m (225). There are 9 atoms per unit cell with the Ni atom at the origin with coordinates (0, 0, 0). The X (Ca, Sr and Ba) atoms are at X1 ($1/4, 3/4, 3/4$), X2 ($1/4, 1/4, 3/4$),

X3 ($\frac{3}{4}, \frac{1}{4}, \frac{3}{4}$), X4 ($\frac{1}{4}, \frac{3}{4}, \frac{1}{4}$), X5 ($\frac{3}{4}, \frac{3}{4}, \frac{1}{4}$), X6 ($\frac{1}{4}, \frac{1}{4}, \frac{3}{4}$), X7 ($\frac{1}{4}, \frac{1}{4}, \frac{1}{4}$) and X8 ($\frac{3}{4}, \frac{3}{4}, \frac{3}{4}$). The fractional atomic coordinates of hydrogen are as follows: H1 ($\frac{1}{4}, 0, 0$), H2 ($\frac{3}{4}, 0, 0$), H3 ($0, \frac{1}{4}, 0$), H4 ($0, \frac{3}{4}, 0$), H4 ($0, 0, \frac{1}{4}$) and H6 ($0, 0, \frac{3}{4}$). The graphs **Figure 2** above show the correlation between the calculated material's total energy (in eV) and unit cell volume (in \AA^3) from electronic structure calculations (black data points) and fitted based on the Murnaghan equation of state (blue or violet curve). The parabolic shape of the curve indicates a minimum at ambient pressure, where the interatomic forces are at equilibrium. The blue line represents the Murnaghan fit a widely employed equation of state that describes the energy-volume relation of a solid under compression or expansion-and allows one to obtain fundamental physical properties. The equilibrium volume corresponding to the minimum of the fitted parabolic **Figure 2(a)** curve is approximately $V_0 = 315 \text{ \AA}^3$, with a corresponding energy of $E_0 = -13818.1 \text{ eV}$, obtained directly from the parabola's minimum. More pronounced curvature indicates a higher bulk modulus B_0 , reflecting increased stiffness of the material. **Figure 2(c)** has a much larger equilibrium volume $V_0 \approx 440 \text{ \AA}^3$ compared to **Figure 2(b)** $V_0 \approx 370 \text{ \AA}^3$ and therefore is less dense. Because the two phases have close equilibrium energies, they are thermodynamically almost equally stable. However, they consist of two different structural phases; **Figure 2(c)** represents an expanded ("swollen") phase compared to **Figure 2(b)**.

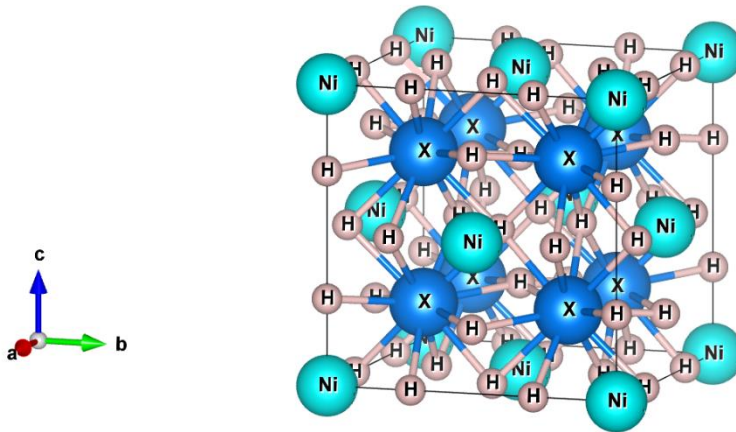
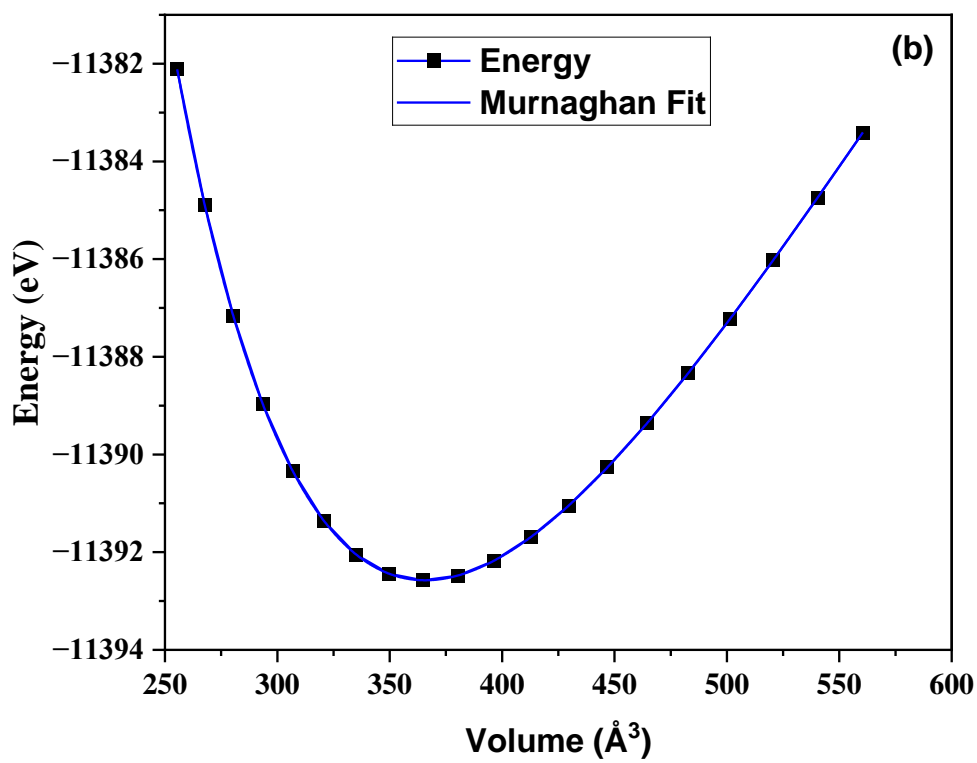
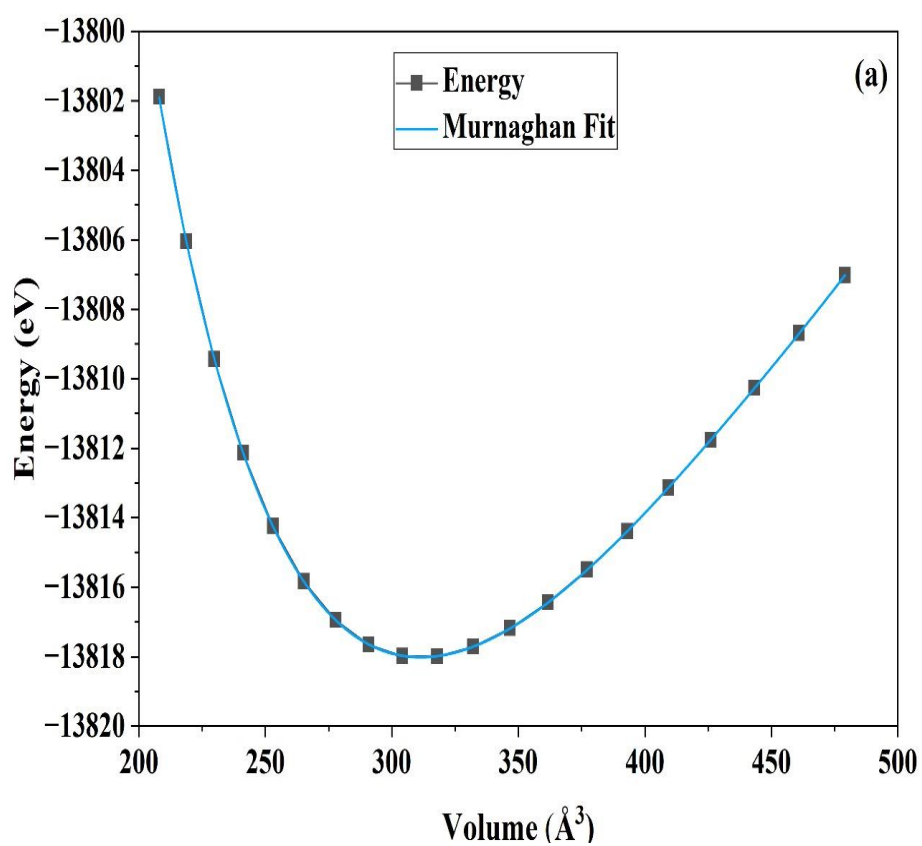


Figure 1: Crystal structure of X_2NiH_6 (X= Ca, Sr and Ba) compounds.



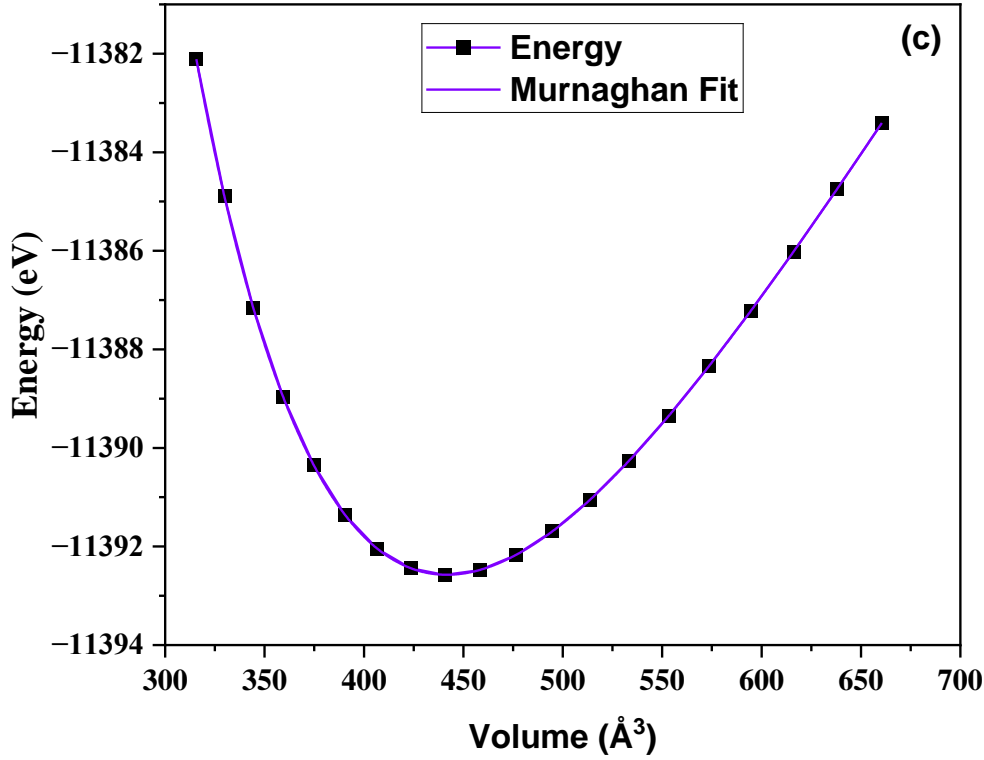


Figure 2: Total energy vs volume curve for optimized (a) Ca_2NiH_6 , (b) Sr_2NiH_6 and (c) Ba_2NiH_6 .

Table 1: The optimized lattice parameter a , volume V , B_0 bulk modulus, and B_0' first derivative of the bulk modulus.

Compounds	a (Å)	V (Å ³)	B_0 (GPa)	B_0' (GPa)
Ca_2NiH_6	6.725	304.142	72.545	3.479
Sr_2NiH_6	7.145	364.759	60.082	3.833
Ba_2NiH_6	7.609	440.537	39.526	4.016

Table 1 represents the ground-state properties of X_2NiH_6 ($\text{X} = \text{Ca}, \text{Sr}, \text{and Ba}$) systems, in terms of their lattice parameter a (Å), volume V (Å³), bulk modulus B_0 , and its first pressure derivative B_0' . Theoretically predicted lattice parameters are 6.725 Å for Ca_2NiH_6 , 7.145 Å for Sr_2NiH_6 , and 7.609 Å for Ba_2NiH_6 . The respective bulk moduli (B_0) are 72.545 GPa for Ca_2NiH_6 , 60.082GPa for Sr_2NiH_6 , and 39.526 GPa for Ba_2NiH_6 . Thus, from the results, Ca_2NiH_6 it is the most compressible and offers the least resistance to compression of these three hydrides.

3.1. Electronic properties

The electronic band structure provides a characteristic fingerprint of a material's behaviour. It comprises two main regions: this bandgap, which distinguishes lower valence bands from upper conduction bands, is equivalent to the energy difference between the conduction band minimum and the valence band maximum [7]. A material's electronic properties are governed by the characteristics of these bands, which delineate the allowed energy ranges for electron occupancy [32]. Understanding the correlation between a material's structure and its properties necessitates an investigation of its electronic behaviour [33]. Calculations are usually made along the high-symmetry points of the first Brillouin zone [11]. In the absence of a band gap, where bands overlap or intersect at the Fermi level, the material exhibits metallic or semi metallic behaviour. in figure 3 An overlap exists between the conduction band (CB) and the valence band (VB) [25], and since neither compound possesses a band gap, the three compounds exhibit metallic behaviour [25]. Moreover, the existence of multiple bands near the Fermi level suggests the possibility of multi-band conductivity, wherein electrons occupying distinct bands collectively contribute to the overall electrical transport [34]. Such a scenario can give rise to intriguing phenomena and complex temperature-dependent transport behaviors [34]. A comprehensive examination of the band crossings at the Fermi level, together with the symmetry characteristics of the associated electronic states, may yield deeper insights into emergent phenomena such as superconductivity and topological behavior, contingent upon the material under investigation. Finally, a detailed investigation of these band crossings and their symmetries may further clarify phenomena such as superconductivity and topological properties, depending on the specific material under consideration. High electronic conductivity enables rapid charge transfer, which in turn promotes hydrogen atom mobility and influences the kinetics of hydrogen uptake and release [35]. The intrinsically high electronic conductivity of metallic materials thus plays a pivotal role in controlling the kinetics of hydrogen permeation through the solid, supporting both storage and release processes [33].

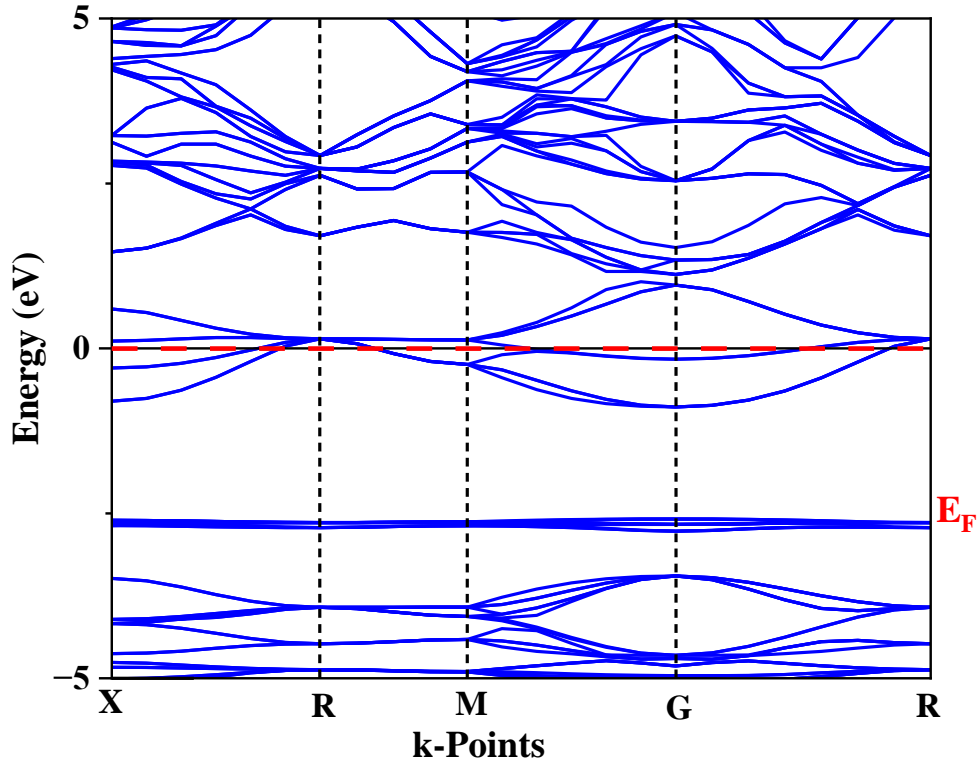
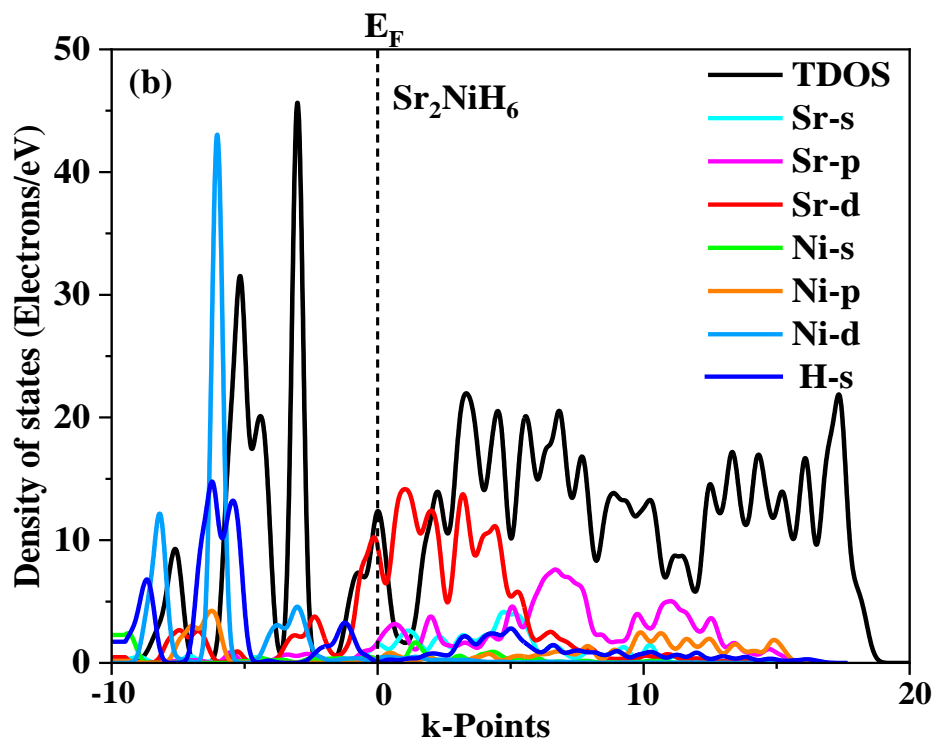
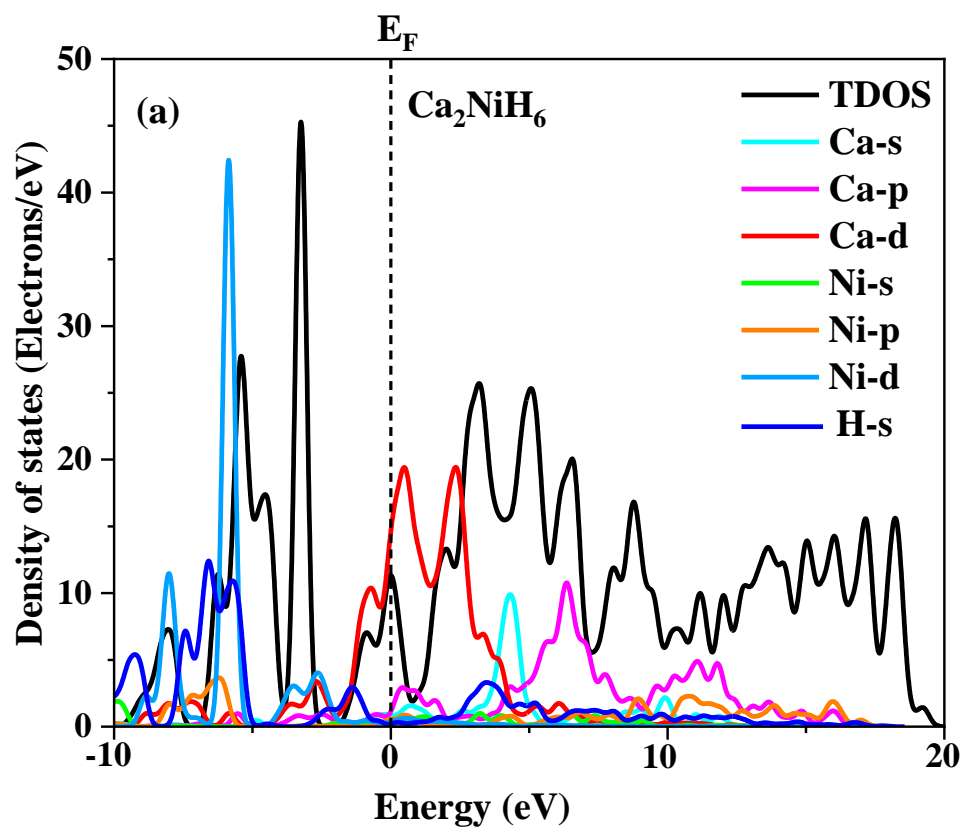


Figure 3: Structure band diagrams for Ca_2NiH_6 , Sr_2NiH_6 and Ba_2NiH_6 .

Figure 4 shows TDOS and PDOS of the three hydrides, The low DOS at the Fermi level of Ca_2NiH_6 , Sr_2NiH_6 and Ba_2NiH_6 indicate that all three of them are conducting in nature. Near the Fermi level states are predominantly of Ni-d and H-s character in all three of them. Ni-d orbitals constitute the major portion of the valence band in Ba_2NiH_6 from -6 eV to -4 eV, with H-s, Ba-s, and Ba-p orbitals appearing in smaller amounts. As in this example, Ca_2NiH_6 also exhibits a very prominent peak within this range owing to the Ni-d orbitals, whereas the H-s, Ca-d, Ca-s, and Ca-p orbitals contribute less at lower energies. Sr_2NiH_6 follows the same trend with Ni-d dominating the -6 eV to -4 eV range with the H-s, Sr-d, Sr-s, and Sr-p orbitals contributing too. Ni-d, H-s, and the respective alkaline earth metal Orbitals-Ba (s, p, d), Ca (s, p, d), and Sr (s, p, d) are all in the conduction band (above 1 eV) for all three compounds. The metal cation contribution differs in all three instances, although the H-s orbitals are distributed across the valence and conduction bands. Ca-d orbitals are relatively more active at the Fermi level, barium orbitals are distributed in the large energy range, and strontium is in between. The conducting or insulating nature of such hydrides is proved by H-s orbitals being present in the whole energy range, but Ni-d orbitals tend to contribute the most in the valence band.



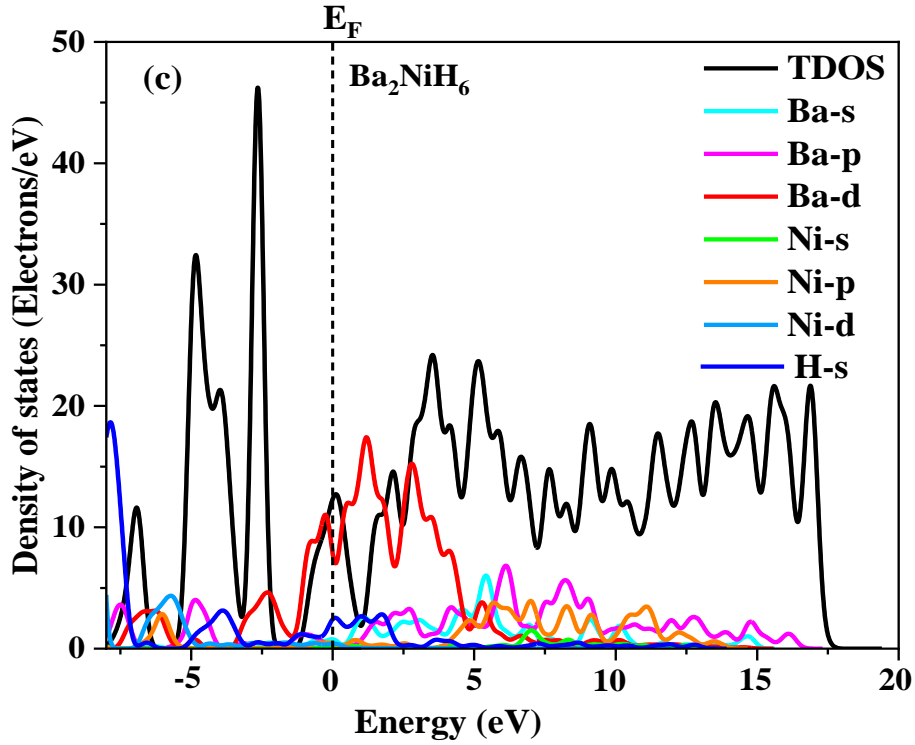


Figure 4: The partial and total DOS are shown for the compounds: (a) Ca_2NiH_6 , (b) Sr_2NiH_6 , and (c) Ba_2NiH_6 .

3.2. Mechanical properties

The mechanical performance of materials, including resistance to stress, load, and pressure, is fundamentally determined by their elastic properties [36]. The elastic properties are essential in applications such as hydrogen storage, where the structural integrity determines the storage capacity and durability of the material [37]. Specific mechanical characteristics, including stiffness, hardness, ductility, and elastic anisotropy, offer valuable information on the material's resistance to deformation and operational reliability. In crystalline networks, elasticity results from the interaction among crystal energy, equilibrium volume, and second-order elastic constants when deformation is applied [35].

In addition, the elastic constants form an intrinsic basis for evaluating the hardness, elastic anisotropy, and also the brittle or ductile nature of the material [38]. Stiffness coefficients like longitudinal stiffness (C_{11}), transverse stiffness (C_{12}), and shear stiffness (C_{44}) are commonly used to describe the mechanical properties of a material [39]. The elastic constant (C_{11}) defines the material's ability to resist uniaxial tensile or compressive deformation, whereas C_{12} characterizes the corresponding transverse strain induced perpendicular to the applied load.

The constant C_{44} represents the material's resistance to shear deformation under an applied shear stress [38]. The mechanical stability of a cubic crystal in its ground state is governed by the Born criteria [38]. These require that $C_{11}>0$, $C_{44}>0$, $C_{11}-C_{12}>0$, and $C_{11}+2C_{12}>0$, the latter being related to volumetric compressibility. For the three hydrides under investigation Ca_2NiH_6 , Sr_2NiH_6 and Ba_2NiH_6 , all elastic constants C_{11} , C_{12} , and C_{44} are positive, with C_{11} significantly exceeding C_{12} , thereby satisfying all four criteria. These results indicate that the studied hydrides are mechanically stable in their respective crystal phases, shown in **Table 2**.

Cauchy pressure, expressed as $C_{12}-C_{44}$ [40], is crucial for comprehending mechanical response [41] and is traditionally applied to find the ductile or brittle nature of a material. Ductility is expressed by a positive value of Cauchy pressure, whereas a negative value shows brittleness [40]. The difference $C_{12}-C_{44}$ is a good quantity to decide the brittleness or ductility of a material. Since this difference is always positive for the compounds studied, the overall tendency is that all three compounds are ductile in the large scales. Specifically, the strontium compound Sr_2NiH_6 is very plastic deformation accommodating in character. A compound's resistance to compression along its crystallographic axes is represented by its axial stiffness (C_{11}). Of the compounds studied, Sr_2NiH_6 recorded the highest C_{11} value of 97.695 GPa, and therefore has high axial rigidity. The lower value of 55.369 GPa is maintained by its counterpart, Ba_2NiH_6 , and is thus best axially flexible. For shear stiffness (C_{44}), Ca_2NiH_6 gives the maximum shear resistance (28.959 GPa), while Ba_2NiH_6 gives the minimum (16.824 GPa). In general, Sr_2NiH_6 is more resistant to compression along one direction of crystallography, whereas Ca_2NiH_6 is most rigid against deformation of its shape. Rigidity of the compounds is dominated by the elastic constants C_{11} and C_{44} . There is an extremely inverse relationship between rigidity and ductility within this series of hydrides.

The bulk modulus (B), shear modulus (G), and Young's modulus are three examples of elastic moduli that represent a material's mechanical response to various modes of deformation. show remarkable differences in the mechanical properties of hydrides Ca_2NiH_6 , Sr_2NiH_6 , and Ba_2NiH_6 (**Table 3**). The bulk modulus (B) is the degree of resistance of the material to volumetric compression under applied pressure [38]. Shear modulus (G) is defined to describe the resistance of the material against transverse deformation with shear stress [38]. Young's modulus (E) defines overall material stiffness [38]. The highest bulk modulus ($B = 82.199$ GPa) is for Sr_2NiH_6 and indicates that it is the least compressible of the three materials. The highest values of Young's modulus ($E = 63.755$ GPa) and shear modulus ($G = 24.592$ GPa) are

for Ca_2NiH_6 and indicate its greater rigidity and resistance to uniaxial stretching and shear deformation. Ba_2NiH_6 has the lowest B, G, and E values and is therefore the most compressible and deformable material in the series.

The Pugh ratio (B/G), a classical standard for ductility, is a key derived value. A material is ductile if the value of B/G is higher than the usual value of 1.75; otherwise, it is brittle [39]. On the basis of ductility and brittleness, the Pugh ratio is above 1.75 for all three hydrides, confirming their inherent ductile nature. While Ba_2NiH_6 and Ca_2NiH_6 take moderate values (2.502 and 2.120, respectively) and are nonetheless ductile, Sr_2NiH_6 is very ductile, with a remarkably high B/G ratio. of 4.769, reflecting high malleability. The most ductile one is Sr_2NiH_6 . Poisson's ratio (ν) is also a measure of the ductility of a material and gives useful information regarding the nature of the interatomic bonding present [42]. In materials with a Poisson's ratio of around 0.1, the dominant bonding is covalent, whereas values typically around 0.25 are characteristic of ionic bonding [42]. The analysis of the Poisson's ratio (ν) reveals that Sr_2NiH_6 exhibits the highest value ($\nu=0.402$), close to the upper theoretical value of 0.5. This is indicative of a high tendency to deform through shear while maintaining the volume almost unchanged, which is the same as having a low effective volumetric compressibility under deformation.

These findings are important for mechanical behavior prediction of such materials in actual conditions such as hydrogen storage, where structural integrity for cyclic pressure and temperature operation is of primary concern. The inverse relationship between the rigidity of Ca_2NiH_6 and the high ductility of Sr_2NiH_6 , confirmed by their elastic constants, moduli, and derived ratios, provides a clear basis for material selection in practical applications.

$$A^u = \frac{2C_{44}}{C_{12}-C_{44}} \quad (1)$$

$$\nu_l = \left[\frac{3B+4G}{3\rho} \right]^{1/2} \quad (2)$$

$$\nu_t = \left[\frac{G}{\rho} \right]^{1/2} \quad (3)$$

$$\nu_m = \left[\frac{1}{3} \left(\frac{1}{\nu_l^3} + \frac{2}{\nu_t^3} \right) \right]^{-1/3} \quad (4)$$

$$\theta_D = \frac{h}{k_B} \left[\frac{3n}{4\pi} \left(\frac{N_A \times \rho}{M} \right) \right]^{1/3} \times \nu_m \quad (5)$$

Where h is Plank's constant (6.626×10^{-34} J.s), K_B is Boltzmann's constant (1.381×10^{-23} J/K), n is the total number of atoms in the unit-cell, N_A is Avogadro's number (6.022×10^{23}), ρ is the density and M is the molar mass [22].

The ultrasonic velocity anisotropy factor (A_u) quantifies the dependence of elastic wave velocities on crystal orientation. A value of $A_u = 1$ describes isotropic acoustic behavior, and any departure from unity quantifies the anisotropy strength the greater the departure from unity, the greater the anisotropy. Of the materials tested, Ca_2NiH_6 exhibits the greatest anisotropy ($A_u = 5.497$) and consequently its acoustic wave velocities vary most with crystallographic direction. Ba_2NiH_6 shows mild anisotropy ($A_u = 2.694$), and Sr_2NiH_6 shows the smallest anisotropy ($A_u = 0.863$) and is nearest to isotropic behavior.

These are the acoustic wave propagation speeds in the materials, namely the longitudinal (v_l) waves, shear (v_t) waves, and mean acoustic velocity (v_m). For Ca_2NiH_6 , wave propagation direction has a considerable influence on the consequent acoustic velocities. Highest velocities in all modes are exhibited by Ca_2NiH_6 , indicating that it is dynamically stiffest and most compressible out of the three compounds, and lowest dynamic rigidity is exhibited by Ba_2NiH_6 .

Debye temperature (θ_D) is a significant physical parameter characterizing vibrational (phonon) behavior of a material. θ_D has a direct proportionality to the mean acoustic speed (v_m) and is the highest temperature at which phonons work. The majority of materials having high θ_D exhibit strong interatomic binding as well as high melting points. In the present series, Ca_2NiH_6 has the highest θ_D (464.638 K), which is a reflection of the strongest interatomic bonding; Sr_2NiH_6 has a mid value (315.745 K), and Ba_2NiH_6 has the lowest θ_D (254.162 K), which is a reflection of the weakest interatomic interactions.

Table 2: Elastic constants C_{jj} (GPa) and Cauchy pressure $C_{12} - C_{44}$ (GPa) calculated values for X_2NiH_6 (X= Ca, Sr and Ba).

Compounds	C_{11}	C_{12}	C_{44}	$C_{12} - C_{44}$
Ca_2NiH_6	77.834	39.312	28.959	10.353
Sr_2NiH_6	97.695	74.451	22.442	52.009
Ba_2NiH_6	55.369	29.313	16.824	12.489

Table 3: Bulk modulus B (GPa), shear modulus G (GPa), Young's modulus E (GPa), B/G and Poisson's ratio ν calculated values for X_2NiH_6 (X=Ca, Sr and Ba).

Compounds	B (GPa)	G (GPa)	E (GPa)	B/G	ν
Ca_2NiH_6	52.153	24.592	63.755	2.120	0.296
Sr_2NiH_6	82.199	17.233	48.323	4.769	0.402
Ba_2NiH_6	37.998	15.186	40.204	2.502	0.323

Table 4: Anisotropic index A^u , longitudinal wave speed v_l (m/s), transverse wave speed v_t (m/s), average wave speed v_m (m/s) and Debye temperature θ_D (K).

Compounds	A^u	v_l	v_t	v_m	θ_D
Ca_2NiH_6	5.497	5532.616	2976.908	3323.567	464.638
Sr_2NiH_6	0.863	5219.262	2112.664	2392.240	315.745
Ba_2NiH_6	2.694	3575.536	1825.701	2045.492	254.162

The **figure 5** presents three-dimensional (3D) plots of various mechanical properties for the three nickel hydrides: Ca_2NiH_6 , Sr_2NiH_6 , and Ba_2NiH_6 , . were generated using ELATE software [43]. In the plot, the directional dependence of the property of interest in the crystal structure is presented.

Young's modulus is a measure of the stiffness of a material under uniaxial tension or compression. The corresponding 3D representations possess bumps along the principal axes and depressions in between, which are slightly different from a perfect spheroid shape. These differences are the anisotropic rigidities of the materials. The [100] directions (main directions) are the directions with the lowest modulus values, indicating lowest stiffness, whereas the [111] directions (diagonals) have highest values, indicating maximum rigidity. Hence, they are more likely to be stretched or compressed more easily in the principal directions ([100], [010], [001]) rather than along the diagonal directions.

Linear compressibility describes the deformation produced by pressure in one direction. The 3D plot of linear compressibility of the three compounds is nearly spherical in nature. This spherical nature indicates that the material is behaving isotropically, and when it's applied with hydrostatic pressure, the volume of the materials responds equally in any direction.

Shear modulus (G) quantifies a material's resistance to shape deformation. The 3D plots reveal complex lobes and clearly non-spherical appearance, reflecting strong anisotropy. Shear is strongly direction-sensitive, and some planes and orientations have little resistance (colored blue) and others have maximum resistance (colored green). For example, in Ba_2NiH_6 and Ca_2NiH_6 , the lowest shear resistance exists along the principal axes ($[100]$), and the maximum resistance is along the $[110]$ directions (between axes).

Poisson's ratio (ν) provides the relative degree of lateral (perpendicular to the applied load) deformation with respect to axial deformation. Of all four mechanical properties studied, the 3D plots of ν are most anisotropic and have the most elongated and irregular shapes. The direction of axial loading exerts a significant influence on the extent of lateral expansion or contraction. Long, sharp lobes in regions of high ν exhibit directions in which a small axial deformation produces a large lateral response, and conversely.

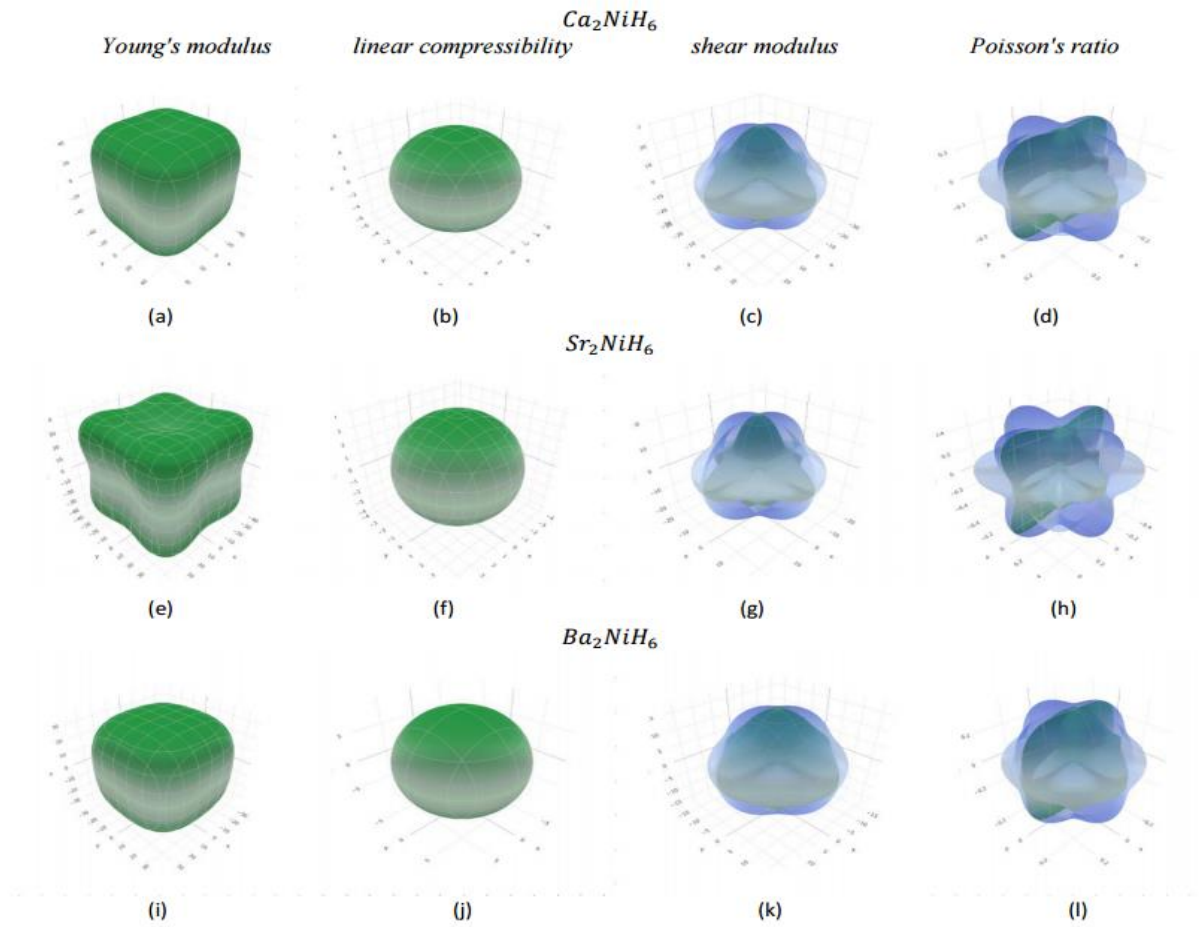


Figure 5 : The anisotropic elastic properties of Ca_2NiH_6 (a, b, c, d), Sr_2NiH_6 (e, f, g, h), and Ba_2NiH_6 (i, j, k, l) are shown in 3D.

3.3. Thermodynamic properties

Using the CASTEP code within the framework of Density Functional Theory (DFT) and employing the Perdew-Burke-Ernzerhof (PBE) [29] functional of the generalized gradient approximation (GGA) [28], **Figure 6** depicts the temperature dependence of entropy, enthalpy, heat capacity, and free energy for the compounds Ca_2NiH_6 , Sr_2NiH_6 and Ba_2NiH_6 .

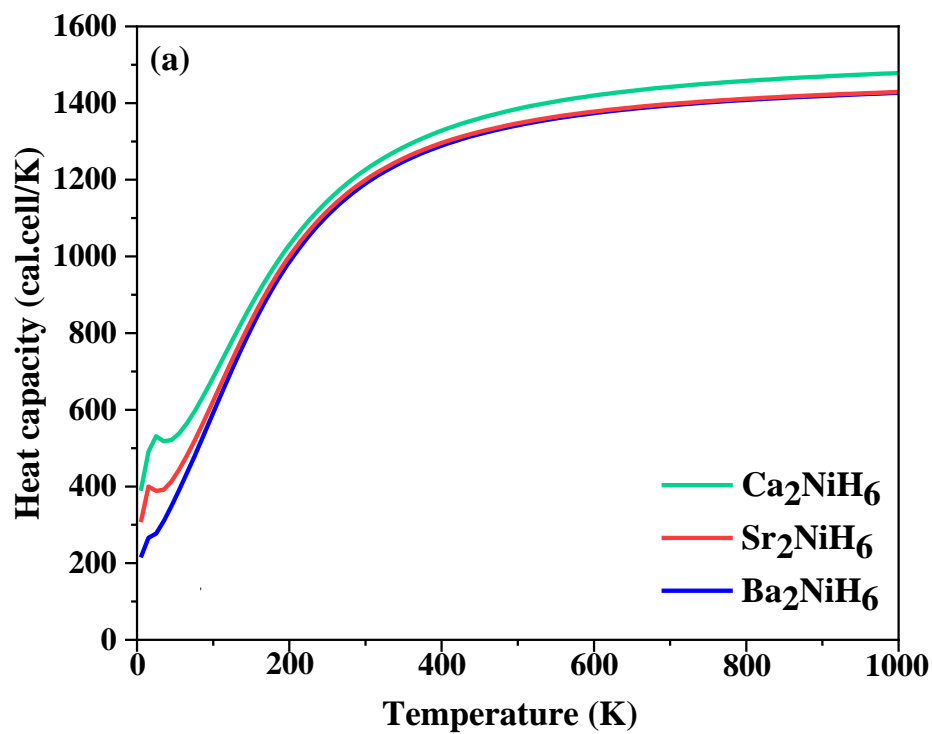
Figure 6(a) shows the temperature dependence of the three hydrides, the increase of their heat capacities with temperature. Heat capacity of a building material refers to the amount of thermal energy the material retains during changes in temperature. It is a measure of the amount of energy required to raise the material's temperature by one degree [44].

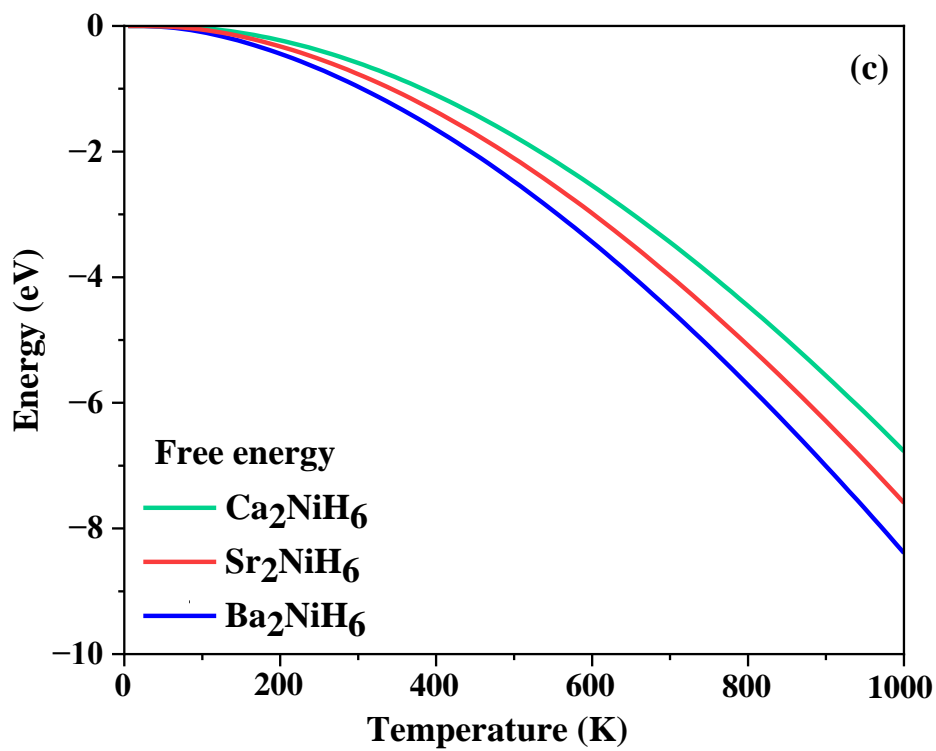
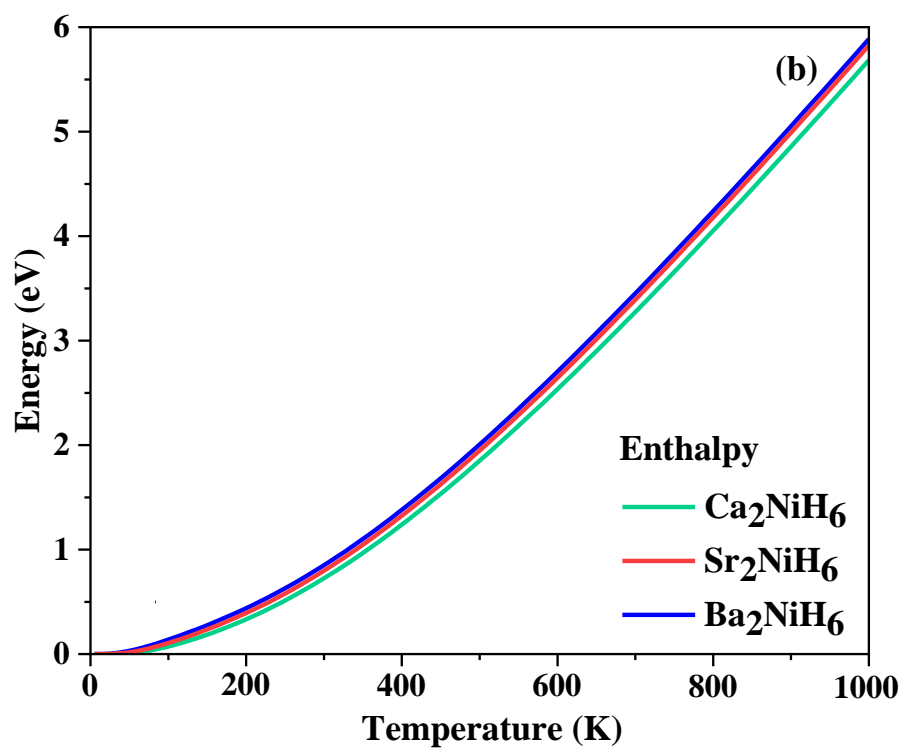
The heat capacities of all the compounds increase with rising temperature, as required by thermodynamic principles. The ability of a substance to store thermal energy is characterized by its heat capacity, a fundamental thermodynamic property [45]. At low temperatures, all the heat capacities are tending towards zero. Ba_2NiH_6 has the lowest heat capacity, followed very closely by Sr_2NiH_6 . In contrast, Ca_2NiH_6 is characterized by a much higher capacity at medium and high temperatures and by a characteristic peak at around 20 K, exhibiting an unusual low-temperature thermal effect. Nevertheless, the material can continue to absorb heat, as its heat capacity increases at low temperatures (0–300 K). Beyond this range, between 300 and 700 K, the heat capacity tends to stabilize [46]. The thermodynamic properties of Ba_2NiH_6 , Sr_2NiH_6 , and Ca_2NiH_6 exhibit clear temperature dependence across the 0–1000 K range. Two extensive fields of structural stability are addressed: the thermodynamic one, which is related to the chemical potential, and the dynamical one. For the three dihydrides, their thermodynamic stability is primarily determined by the formation enthalpy [47].

in **Figure 6(b)** The enthalpy of Ba_2NiH_6 starts near 0 eV at 0 K and increases smoothly and gradually with temperature, reaching approximately 5.8 eV at 1000 K. Enthalpy, a state function, is defined as the sum of a system's internal energy and the product of its pressure and volume. It is mathematically expressed as $\Delta H = E + PV$ [48]. Ca_2NiH_6 shows a similar trend, though with consistently lower enthalpy values, rising to about 5.6 eV at 1000 K. Sr_2NiH_6 displays enthalpy behavior comparable to Ba_2NiH_6 and Ca_2NiH_6 , starting near 0 eV and increasing to roughly 5.7 eV at 1000 K.

In terms of free energy, as seen in **Figure 6(c)**, we have Ba_2NiH_6 decreases from 0 eV at 0 K to approximately –8.5 eV at 1000 K, with the rate of decrease becoming steeper at higher temperatures. Ca_2NiH_6 exhibits a similar temperature dependence, albeit with less negative values, reaching around –7.0 eV at 1000 K. Sr_2NiH_6 falls between the other two, with a free energy of about –7.7 eV at 1000 K. Negative values of Gibbs free energy indicate the thermodynamic stability of a material [48]. **Figure 6(d)** shows Entropy for all three compounds increases with temperature, in accordance with the third law of thermodynamics. Ba_2NiH_6 displays a nonlinear rise in entropy from 0 eV at 0 K to approximately 14.3 eV at 1000 K. Ca_2NiH_6 again follows a similar pattern but reaches a lower maximum entropy of about 12.6 eV. Sr_2NiH_6 has intermediate values, with entropy rising to nearly 13.4 eV at 1000 K. The entropy change occurring during hydrogen adsorption and desorption governs both the reversibility and the kinetics of the hydrogen storage process [35]. Specifically, the change in entropy (ΔS) reflects the degree of disorder associated with hydrogen release, as typically

observed during gas evolution due to the higher entropy of hydrogen in the gaseous state compared to the solid phase [49].





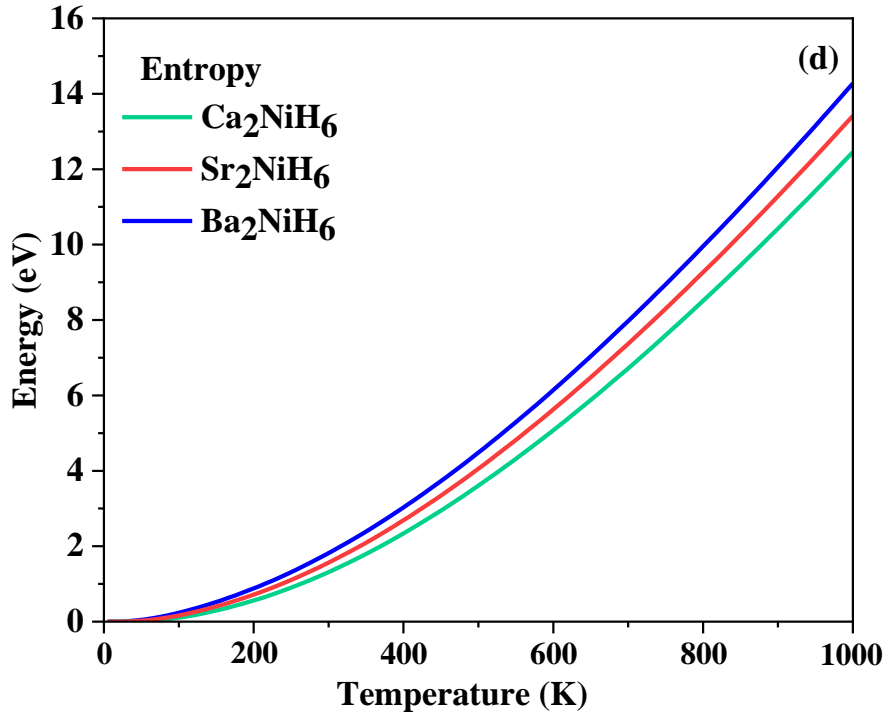


Figure 6: Thermodynamic properties the variation of (a) Thermal capacity, (b) Enthalpy, (c) Free energy and (d) Entropy as a function temperature for Ca_2NiH_6 , Sr_2NiH_6 and Ba_2NiH_6 .

3.4. Optic properties

Understanding the optical properties of a material is essential for analyzing its response to incident electromagnetic waves and is equally critical for evaluating its potential applications in optoelectronic and photovoltaic devices [6].

A material's response to incident electromagnetic radiation is determined by its optical properties, with its response to visible light being particularly critical for optoelectronic applications [50]. The real component ($\epsilon_1(\omega)$) and the imaginary component ($\epsilon_2(\omega)$) of the dielectric function are employed to determine the absorption coefficient $\alpha(\omega)$, reflectivity $R(\omega)$, refractive index $n(\omega)$, extinction coefficient $k(\omega)$, and optical conductivity $\sigma(\omega)$ [40].

Figure 7 is the optical behavior of Ba_2NiH_6 , Ca_2NiH_6 and Sr_2NiH_6 . In **Figure 7(a)**, the real part of the dielectric function $\epsilon_1(\omega)$ of Ba_2NiH_6 has a strongly positive value at energies less than 1 eV, indicative of a strong response to polarization. The value drops quickly and becomes negative between approximately 1 eV and 3 eV, characteristic of materials near plasma frequencies, where the electric field created by the incident oscillates out of phase with it.

Above this, $\epsilon_1(\omega)$ becomes oscillatory in nature, with maxima and minima at 7 eV and 29 eV, before reaching unity above 35 eV. Contrary to this, Ca_2NiH_6 starts with a smaller value for low energies, becomes negative by 1–2 eV, and creates oscillatory maxima at 3 eV, 7 eV, and 20 eV, reaching eventually to 1 for high energies. Sr_2NiH_6 begins at a tiny positive value, becomes negative at 1–2 eV, and possesses an identical oscillatory shape with peaks at 3 eV, 7 eV, and 22 eV, again tending towards unity at higher energy. **Figure 7(b)** presents the imaginary part of the dielectric function $\epsilon_2(\omega)$, which directly relates to the material's absorption characteristics. For Ba_2NiH_6 , there is one major high-intensity peak at 31 eV, in agreement with earlier absorption measurements, and very weak peaks at 2 eV, 7 eV, and 23 eV. Ca_2NiH_6 consists of peaks at 3 eV and 7 eV, in addition to a broader feature peaking at 20 eV, although this with decreased intensity compared to Ba_2NiH_6 . Sr_2NiH_6 also has a very similar $\epsilon_2(\omega)$ profile to Ca_2NiH_6 , with similar intensities of peak absorption at 3 eV, 7 eV, and 22 eV. The text accounts for the way polarization and wave velocity of electromagnetic waves within a material depend on the real component of the dielectric constant, whereas the imaginary component provides details on the absorption of energy by the material. The dielectric constant $\epsilon(\omega)$ is influenced by intraband electronic transitions, significant at low energies, and interband transitions, with high reliance on the electronic structure of the material [50]. This can be determined by the complex dielectric function, which is given by: $\epsilon(\omega) = \epsilon_1(\omega) + i\epsilon_2(\omega)$ [51].

In absorption $\alpha(\omega)$ (**Figure 7(c)**), reflectivity $R(\omega)$ (**Figure 7(d)**), refractive index $n(\omega)$ (**Figure 7(g)**) and extinction coefficient **Figure 7(h)** This can be determined by the complex dielectric function, which is given by $\epsilon(\omega) = \epsilon_1(\omega) + i\epsilon_2(\omega)$.

$$\alpha(\omega) = \sqrt{2}\omega \left[\sqrt{\epsilon_1^2(\omega) + \epsilon_2^2(\omega)} - \epsilon_1(\omega) \right]^{\frac{1}{2}} \quad (6)$$

$$R(\omega) = \left| \frac{\sqrt{\epsilon_1(\omega) + j\epsilon_2(\omega)} - 1}{\sqrt{\epsilon_1(\omega) + j\epsilon_2(\omega)} + 1} \right|^2 \quad (7)$$

$$n(\omega) = \frac{1}{\sqrt{2}} \left[\sqrt{\epsilon_1^2(\omega) + \epsilon_2^2(\omega)} + \epsilon_1(\omega) \right]^{\frac{1}{2}} \quad (8)$$

$$K(\omega) = \frac{1}{\sqrt{2}} \left[\sqrt{\epsilon_1^2(\omega) + \epsilon_2^2(\omega)} - \epsilon_1(\omega) \right]^{\frac{1}{2}} \quad (9)$$

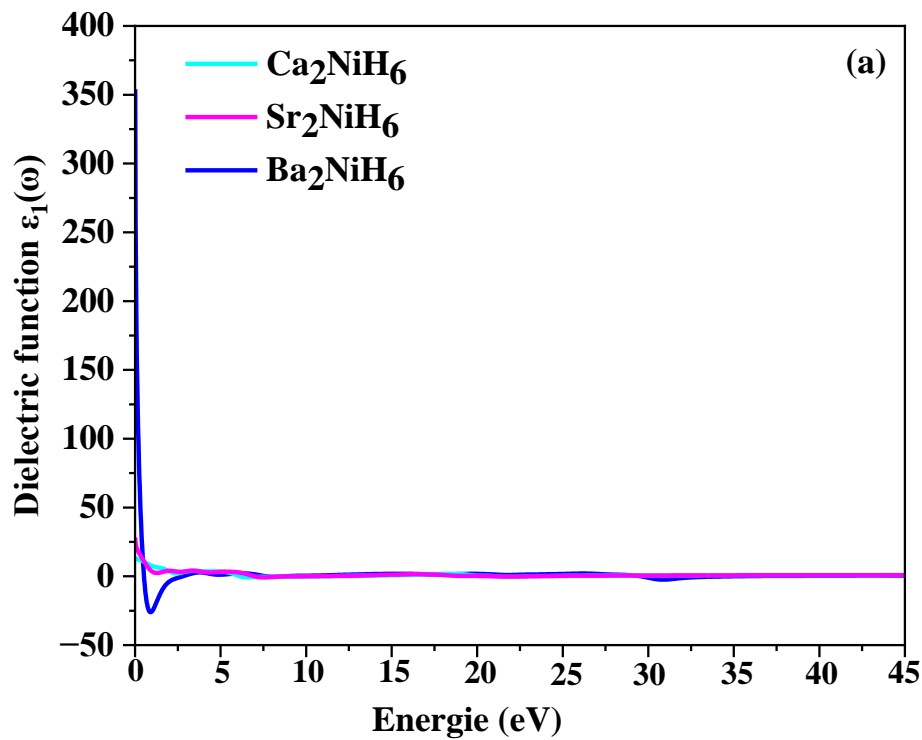
From the absorption spectra (**Fig. 7a**), Ba_2NiH_6 has a narrow and intense peak around 31 eV, with intense photon absorption at the energy. Other than the major peak at around 31 eV, there are also low absorptions at around 7 eV and 35 eV. Ca_2NiH_6 , on the other hand, possesses a

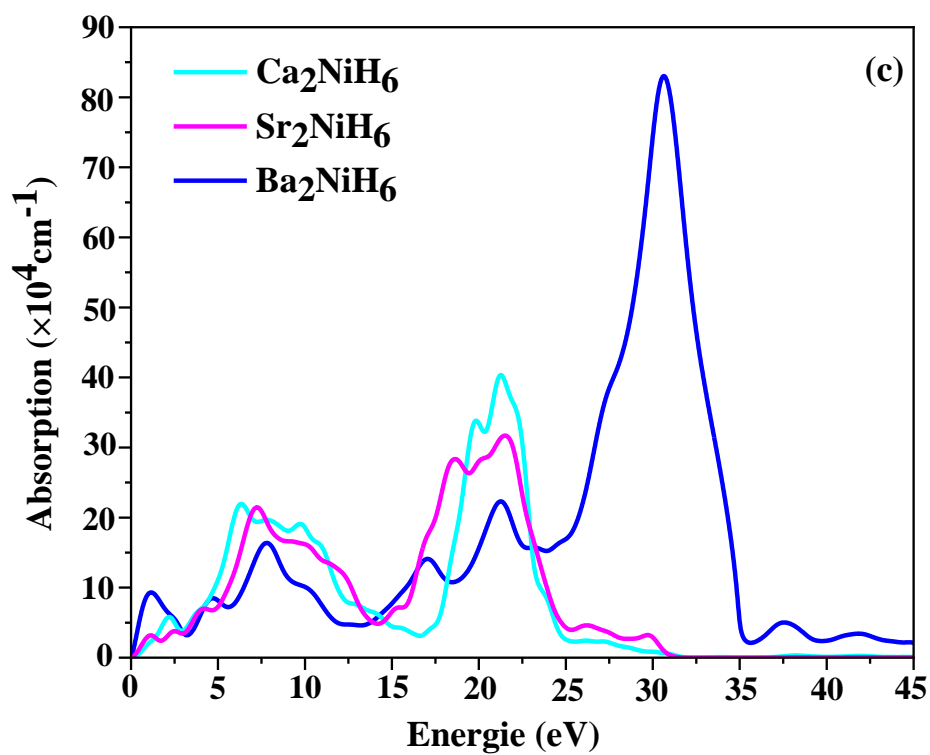
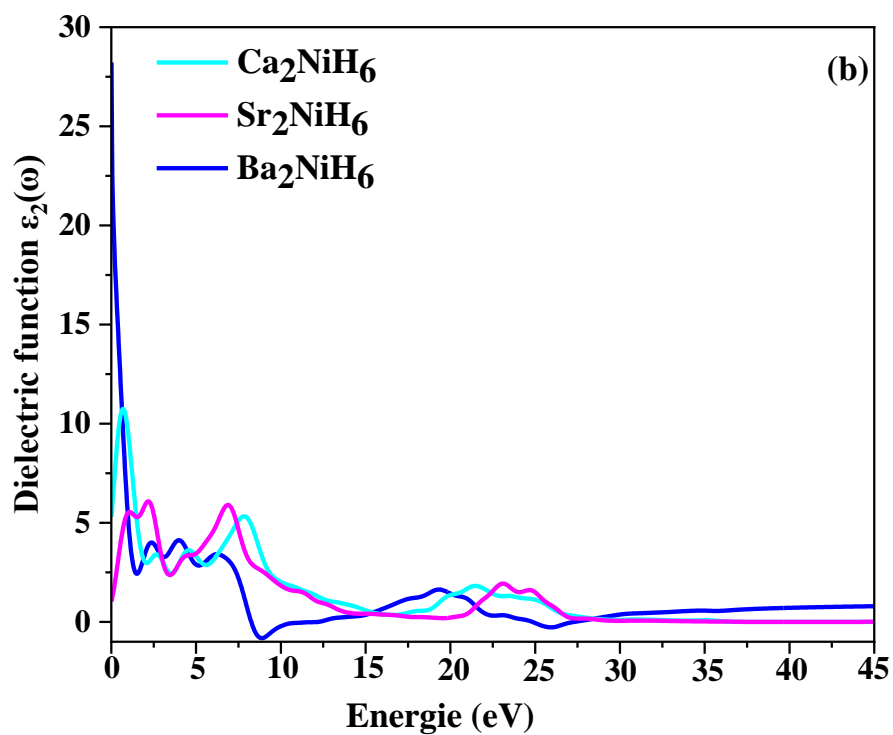
number of low-energy absorption peaks with the strongest at 7 eV and 20 eV, while its high-energy absorption is overall less intense than that of Ba_2NiH_6 . Sr_2NiH_6 shows similar low-energy peaks of absorption to Ca_2NiH_6 at 7 eV and 22 eV, and similarly weaker absorption at higher energies compared to Ba_2NiH_6 . Reflectivity spectra (**Figure 7(d)**) share a strong correspondence with absorption's behavior. Ba_2NiH_6 features a broad peak in reflectivity around 31 eV due to its strong absorption, combined with strong reflectance at smaller energies, particularly below 2 eV and around 23 eV. Ca_2NiH_6 also shows major peaks in reflectivity around 3 eV, 8 eV, and 20 eV in coincidence with the position of its absorption features but at reduced reflectivity than Ba_2NiH_6 at higher energies. The same trend is seen for Sr_2NiH_6 , having peaks in reflectivity at ca. 3 eV, 8 eV, and 22 eV but at lower reflectivity at high energies than Ba_2NiH_6 . For optoelectronic and photovoltaic uses, it is desirable to consider the material's response within the visible, ultraviolet, and infrared spectral ranges [6]. **Figures (7(e)-7(f)-7(g)-7(h))** present the optical response of Ba_2NiH_6 , Ca_2NiH_6 and Sr_2NiH_6 , specifically the real and imaginary components of optical conductivity, refractive index, and extinction coefficient versus photon energy.

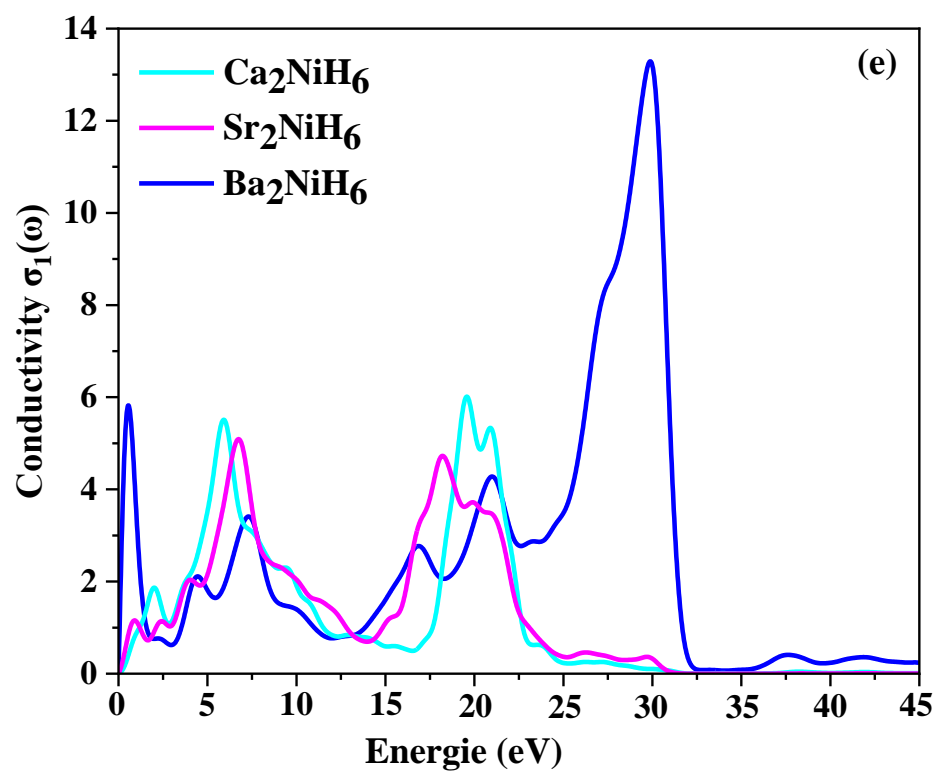
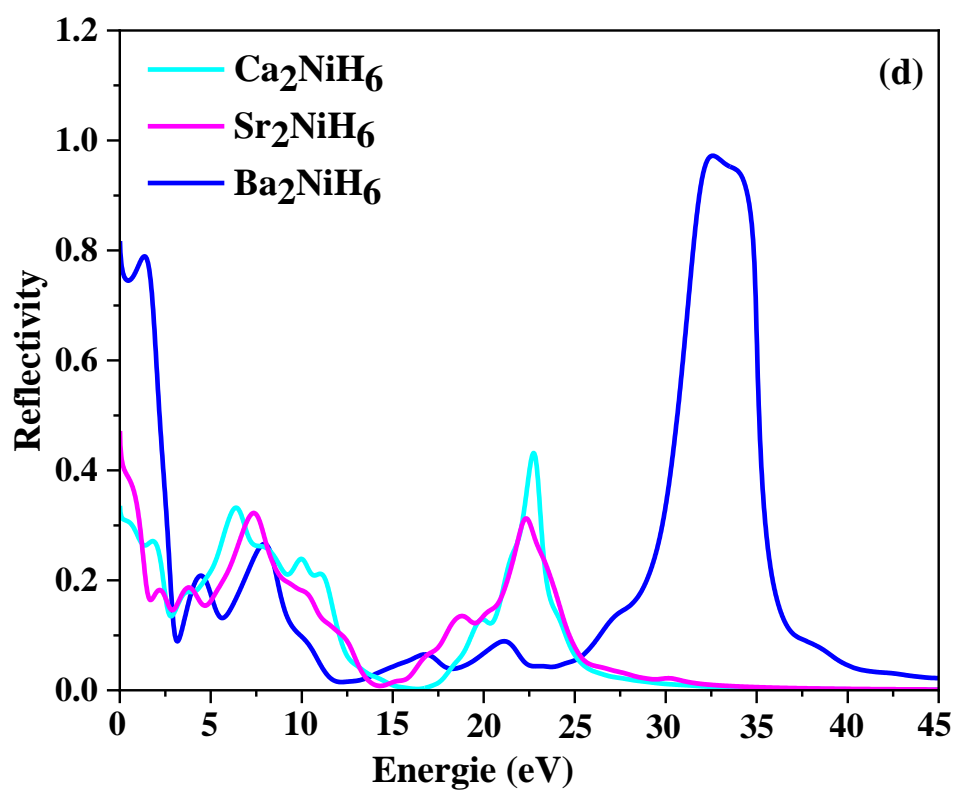
Ba_2NiH_6 , in **Figure 7(e)**, presenting the real part of the optical conductivity $\sigma_1(\omega)$, has a strong and broad peak at about 31 eV, as in agreement with its large absorption at this energy. There are also other small peaks at 2 eV, 7 eV, and 23 eV. Ca_2NiH_6 also has peaks at 3 eV, 7 eV, and a smaller one at 20 eV, although not as intense as the major peak of Ba_2NiH_6 . Similarly, Sr_2NiH_6 also has peaks at 3 eV, 7 eV, and 22 eV, almost the same as that of Ca_2NiH_6 .

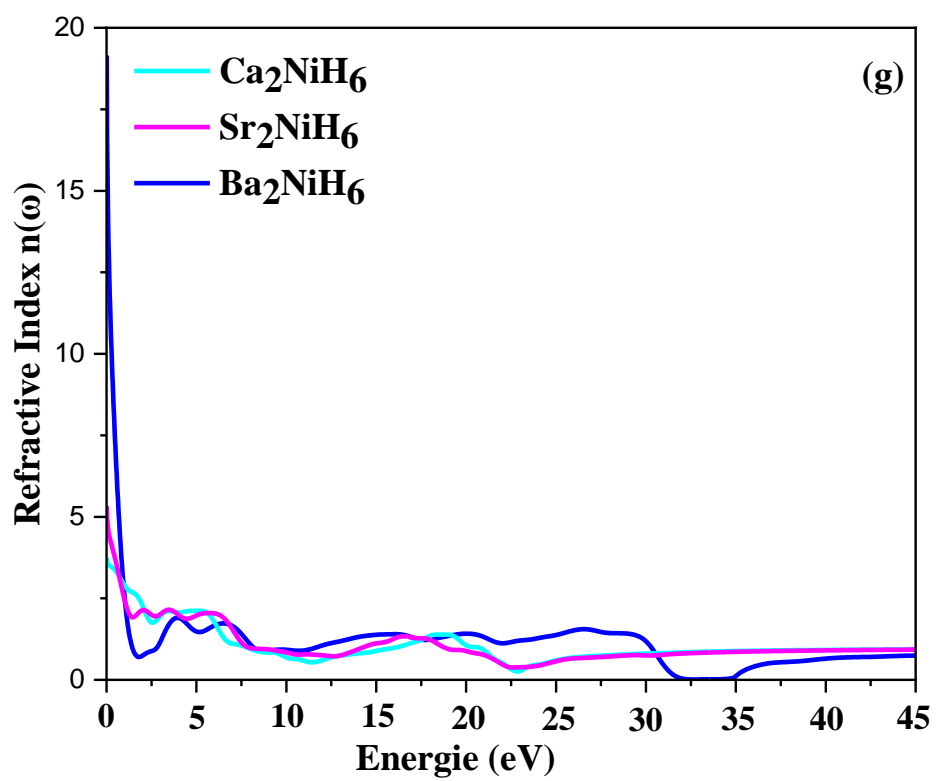
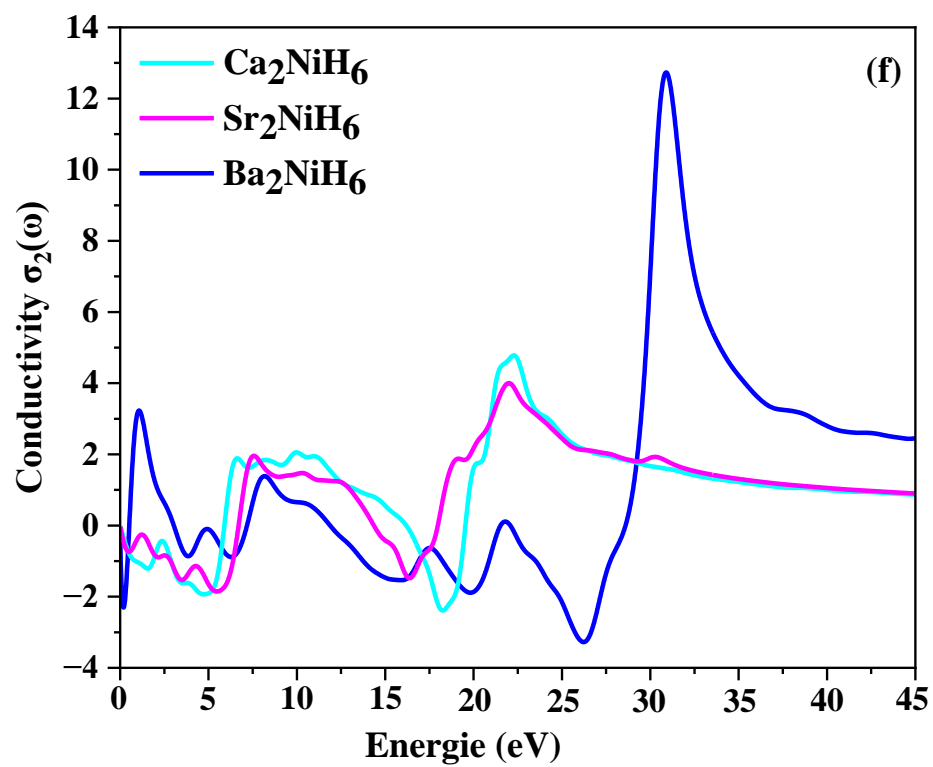
Figure 7(f) is a plot of the imaginary part of the optical conductivity $\sigma_2(\omega)$, which is associated with dispersion and energy storage. Ba_2NiH_6 has $\sigma_2(\omega)$ varying both strongly and crossing zero near 31 eV, corresponding to the maximum in $\sigma_1(\omega)$ and exhibiting resonant absorption. Ca_2NiH_6 and Sr_2NiH_6 exhibit analogous synchronized oscillation in $\sigma_2(\omega)$ for their $\sigma_1(\omega)$ maxima, but these are less strong than in Ba_2NiH_6 . has effective energy absorption, favorable electronic transitions, and a strong interaction with electromagnetic fields that together contribute to improved hydrogen adsorption desorption kinetics and increased storage capacity [52]. Photons are slowed down as they enter a substance via interactions with electrons, resulting in a refractive index greater than 1, Higher refractive index materials, have more photon delay as light passes through them, Raising the electrical densities within a substance also increases the value of the refractive index [6]. **Figure 7(g)** gives the refractive index $n(\omega)$. A very important consideration in the determination of the amount of bending of light, especially in photoelectric fields, is the refractive index [6]. Ba_2NiH_6 possesses an extremely

high refractive index below energy of 1 eV, which later steeply falls off. It is having maxima and minima at 3 eV, 7 eV, 17 eV, and 29 eV, later rising towards 1 beyond energy level of 35 eV. Ca_2NiH_6 and Sr_2NiH_6 both possess lower values at low energy with peaks at 3 eV, 7 eV, and 20–22 eV, finally tending to 1 for higher energies as well. In **Figure 7(h)** is the extinction coefficient, which is an indication of how much light is scattered or absorbed per unit of distance. Ba_2NiH_6 has a very strong peak around 31 eV, reflecting its high absorption, accompanied by smaller peaks at 2 eV, 7 eV, and 23 eV. Ca_2NiH_6 has peaks at 3 eV, 7 eV, and an extended feature at 20 eV, typically lower in intensity than Ba_2NiH_6 . Sr_2NiH_6 exhibits twin behavior to Ca_2NiH_6 with maxima for extinction coefficients of 3 eV, 7 eV, and 22 eV, and with intensity of comparable order.









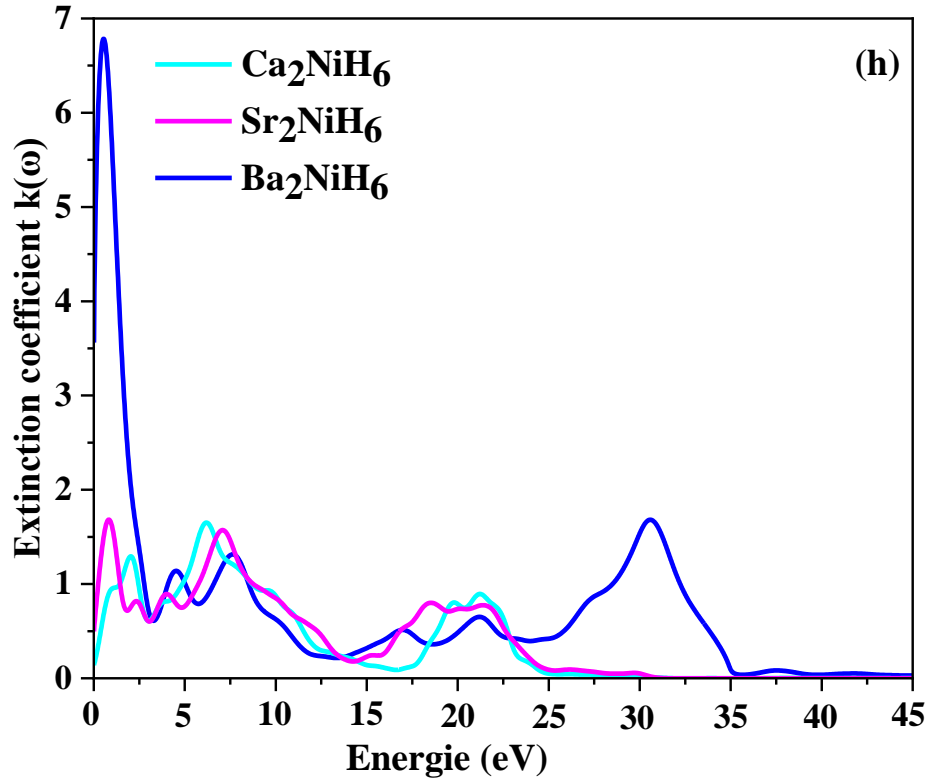
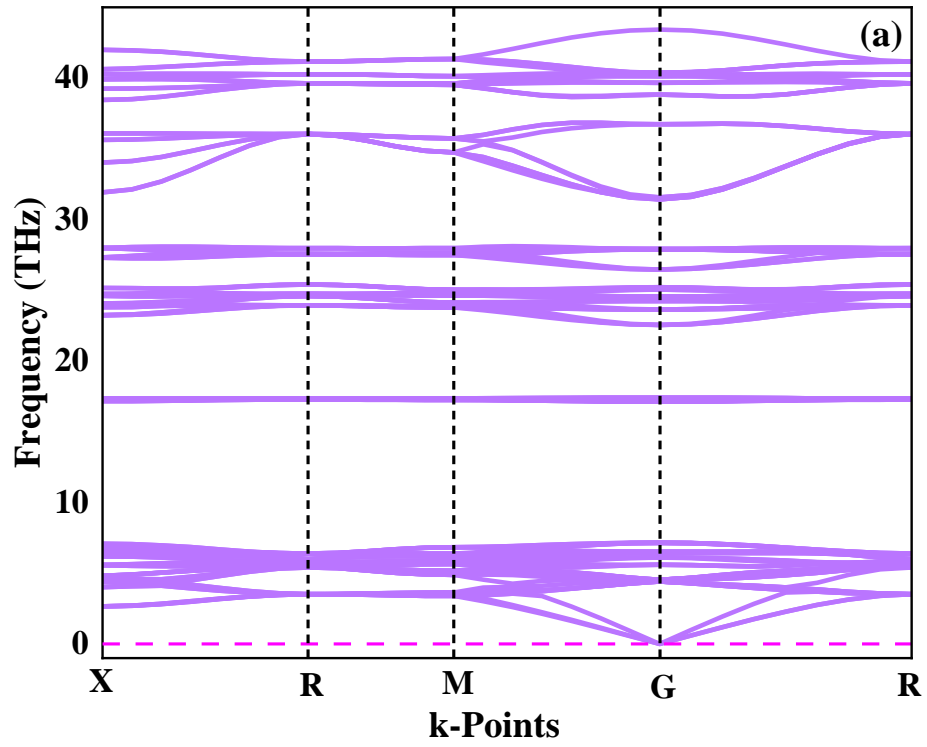


Figure 7: The calculated variation of (a) real dielectric function $\epsilon_1(\omega)$, (b) imaginary dielectric $\epsilon_2(\omega)$, (c) Absorption $\alpha(\omega)$, (d) Reflectivity $R(\omega)$, (e) real Conductivity $\sigma_1(\omega)$, (f) imaginary conductivity $\sigma_2(\omega)$, (g) Refractive index $n(\omega)$ and (h) Extinction coefficient $k(\omega)$ as a function of photon energy for the compounds Ca_2NiH_6 , Sr_2NiH_6 and Ba_2NiH_6 .

3.5. Phonon State Density and Phonon Dispersion

The area of crystal materials is where the phonon behavior plays a highly important part. Physical properties of the material are directly or indirectly quantified through phonon dispersion spectra [53]. Phonon dispersion spectra explain all structural equilibrium, phase transition, and vibrational contribution to the thermal energy and charge transport behavior of a material [53]. The interaction of phonons with hydrogen may determine the efficiency of the material to absorb and release hydrogen [3]. The phonon dispersion curves in **Figure 8** indicate the vibrational characteristics of the material, which are significant to determine for understanding its thermal stability and hydrogen storage capacity [3]. These three acoustic branches of this given phonon band structure are seen from zero frequency at the 'G' point. There is a multi-atom primitive unit cell evident in that there are many optical branches at higher frequencies. Thus, no negative frequencies are seen, revealing that all three hydrides are

dynamically stable [7]. unexpectedly, the phonon dispersion curves contain no imaginary frequencies, and all the values on the curves are positive, providing thermodynamic stability for all materials [54]. The dynamic stability of the compounds results from the absence of imaginary frequencies in the phonon dispersion curves [10].



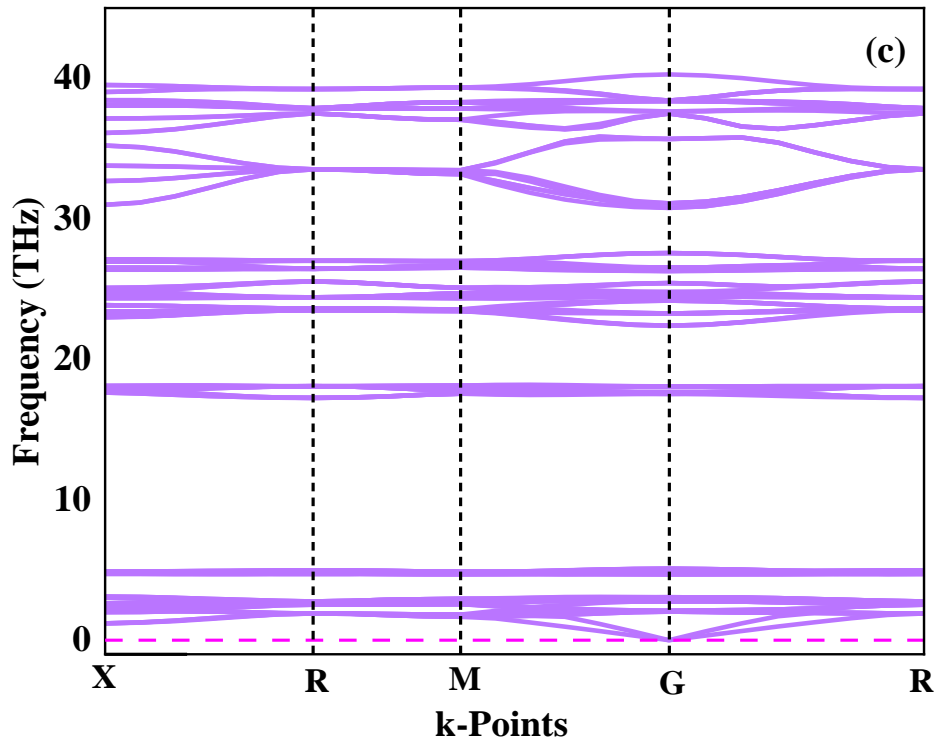
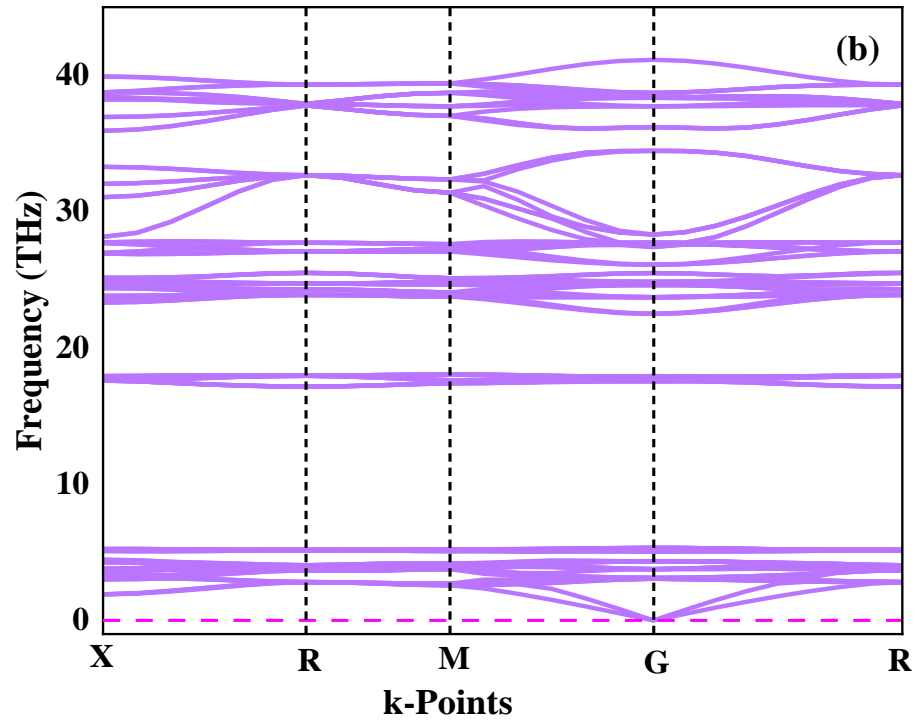
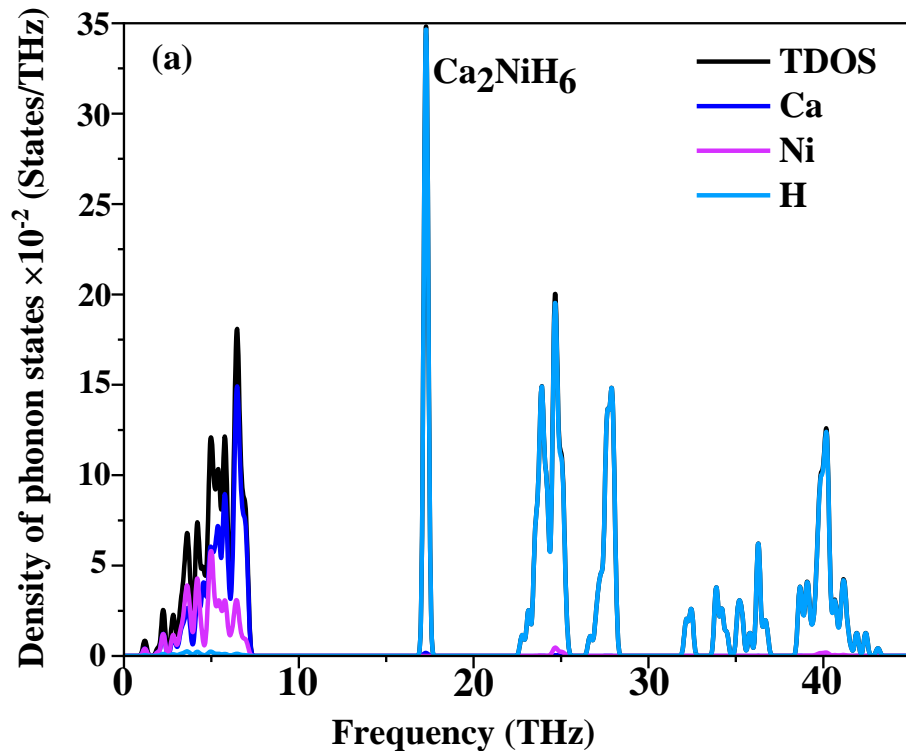


Figure 8: Phonon dispersion for (a) Ca_2NiH_6 , (b) Sr_2NiH_6 and (c) Ba_2NiH_6 .

Figure 9 illustrates the DOS phonon plots, which give us a better image of the vibration behavior of such metal hydrides. Atoms of heavy metals contribute mostly to the low-frequency modes, while hydrogen vibration determines the high-frequency patterns. From these numbers, high-frequency phonons are mostly the result of lighter atoms, and low-frequency phonons are mostly the result of vibration of heavier atoms [55]. This work follows the general rule that lighter atoms possess higher vibrational frequencies [56].

Ba_2NiH_6 contains sharply defined peaks for Ni at 5–15 THz and a rather broad band of Ba modes at the low frequencies. There are a few sharp peaks at the higher frequencies where the hydrogen modes are clustered. Ca_2NiH_6 at around 20 THz has a very high and sharp peak for hydrogen, indicating that the phase has a very dissimilar vibrational mode for hydrogen. The contribution of Ni is not as visible as the other two, while the Ca modes occur lower in frequency. Low-frequency behavior in Sr_2NiH_6 is observed with high contribution from Sr, reaching frequencies above slightly for Ba in Ba_2NiH_6 . The hydrogen modes span an interval of high frequency, and Ni contribution is seen in the intermediate interval.



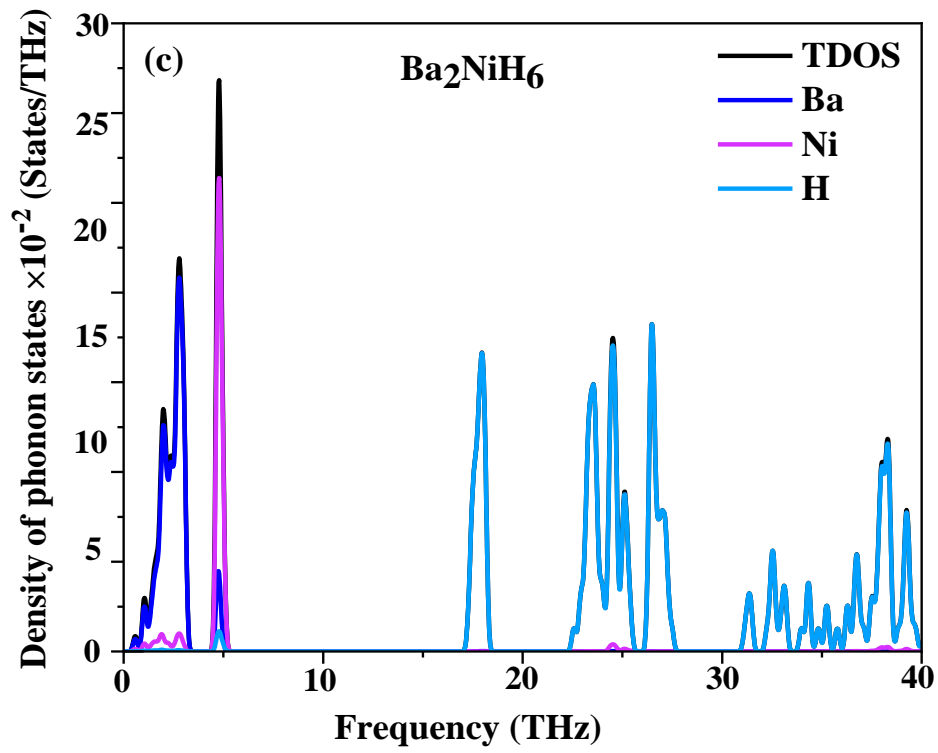
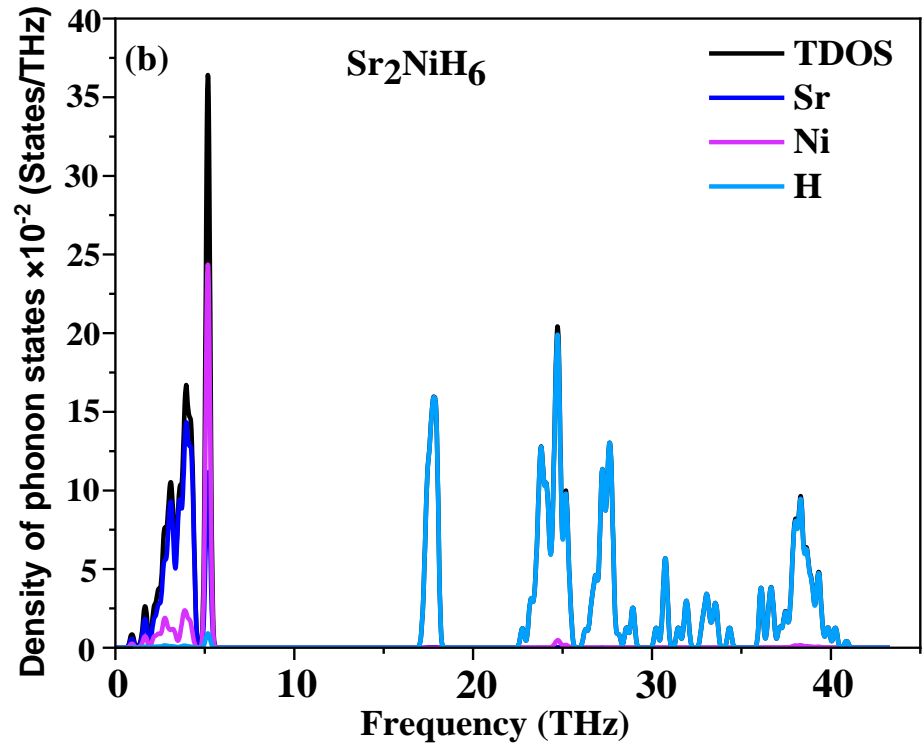


Figure 9: Phonon state density for (a) Ca_2NiH_6 , (b) Sr_2NiH_6 and (c) Ba_2NiH_6

3.6. Hydrogen Storage Capacity and Desorption Behavior

Understanding the hydrogen storage capacity of complex hydrides is crucial in the design of solid-state hydrogen storage devices. With good gravimetric hydrogen storage capacity, positive stoichiometry, and light-element composition reported for ternary hydrides of the type X_2NiH_6 ($X = Ca, Sr$ and Ba), these are very promising candidates. To assess in the context of thermodynamics, formation energies and hydrogen composition were computed to study their potential application. This issue must be addressed before hydrogen can be properly utilized for storage. Although there are various storage methods, the solid, liquid, and gaseous forms are most common [57]. The most promising solution to overcoming this issue is the successful implementation of a system capable of reversibly storing and releasing hydrogen in large quantities [57]. **Table 5** summarizes the formation energies and hydrogen capacity of the studied materials. Thermodynamic stability is quantification of the tendency of a system to stay at its equilibrium state. Materials are stable if the calculated formation energy is negative; otherwise, any positive value means it is not stable [58].

The energy of formation has been determined by equation (10) [40]:

$$\Delta E_f = \frac{E_{tot}(X_2NiH_6) - 2E_{tot}(X) - E_{tot}(Ni) - 3E_{tot}(H_2)}{N} \quad (10)$$

With $E_{tot}(X_2NiH_6)$ present the total energy of X_2NiH_6 , while $E_{tot}(X)$, $E_{tot}(Ni)$ and $E_{tot}(H_2)$ represent the total energies of the atoms X (Ca, Sr and Ba), Ni and H_2 . N is the total number of atoms in the unit (X_2NiH_6). The results show that the materials are stable based on the negative values. Ca_2NiH_6 has the lowest formation energy, indicating the highest thermodynamic stability of the compounds under investigation, followed by Sr_2NiH_6 .

The following equation (11) [59] was used to determine the hydrogen storage capacity:

$$C_{wt\%} = \left(\frac{\left(\frac{H}{M}\right)M_H}{M_{host} + \left(\frac{H}{M}\right)M_H} \right) \times 100 \quad (11)$$

With H/M the atomic ratio between the hydrogen atoms and the host material. M_H and M_{host} are the molar masses of the hydrogen and hydride under study. The complex hydrides are of very significant importance in hydrogen storage, and the calculated hydrogen storage capacities of Ca_2NiH_6 , Sr_2NiH_6 , and Ba_2NiH_6 are 4.005 wt%, 2.548 wt%, and 1.750 wt%, respectively.

Among them, Ca_2NiH_6 has the highest hydrogen storage capacity, followed by Sr_2NiH_6 , and Ba_2NiH_6 has the lowest. The experiments show that Ca_2NiH_6 is a very promising material for future hydrogen storage due to its high gravimetric capacity.

Table 5: The optimum formation energy ΔE_f and hydrogen storage capacity C (wt%).

Compounds	ΔE_f (eV/atom)	C (wt%)
Ca_2NiH_6	-0,512	4.006
Sr_2NiH_6	-0,418	2.458
Ba_2NiH_6	-0,404	1.750

4. Conclusion

This research extensively explored the structural, mechanical, thermodynamic, and phononic characteristics of the complex hydrides X_2NiH_6 ($\text{X} = \text{Ca}, \text{Sr}$ and Ba) using first-principles Density Functional Theory (DFT) calculations. All three compounds, thermodynamic calculations show, exhibit an increase in heat capacity and entropy with temperature, as would be expected by simple thermodynamic considerations. Enthalpy and Gibbs free energy calculations illustrate that materials with negative formation energies that become more and more negative with increasing temperature are thermodynamically stable. Moreover, variations of entropy for hydrogen adsorption and desorption were also found to be the key factors controlling reversibility and kinetics of the hydrogen storage reaction. In addition, computation of the optical properties like energy-dependent dielectric function and refractive index indicates that Ba_2NiH_6 possesses a high refractive index at low energies of photons, while Ca_2NiH_6 and Sr_2NiH_6 retain relatively low values. As a whole, comparative investigation of Ca_2NiH_6 , Sr_2NiH_6 and Ba_2NiH_6 occupies a crucial role in their dynamical stability, mechanical stability, and capability for hydrogen storage. Of all these, Ca_2NiH_6 is recognized as the most qualified candidate for real application for hydrogen storage. Phonon dispersion curves indicate the inherent vibrational properties of the compounds studied, which are measures of their thermal and dynamic stability. Absence of imaginary frequencies in such spectra lends support to the thermodynamic stability of all the materials under investigation. According to the data, showing calculated formation energy and hydrogen storage capacities for the studied hydrides,

Ca_2NiH_6 is thermodynamically most stable among the considered compounds. The calculated values of storage capacities equal to 4.005 wt%, 2.548 wt%, and 1.750 wt% for Ca_2NiH_6 , Sr_2NiH_6 , and Ba_2NiH_6 are other evidence of the important roles of hydrides perovskite in hydrogen storage technology.

References:

- [1] Ramalingam K, Kandasamy M, Subbiah G, Vellaiyan S, Devarajan Y, Chandran D, Raviadarar R. Energy, environmental, and economic benefits of hydrogen-enriched biofuel using ammonium hydroxide in reactivity-controlled compression ignition engines. *Results Eng.* 2024;24:103672.
- [2] Mwakipunda GC, Kouassi AKF, Ayimadu ET, Komba NA, Nadege MN, Mgimba MM, et al. Underground hydrogen storage in geological formations: A review. *J Rock Mech Geotech Eng.* 2025.
- [3] Moharam MM, Saleh EAM, Sabeen S, Hussain K, Alshik NM, Nabil GM, et al. Multifaceted exploration of structural, optoelectronic, mechanical, bader charge, phononic, and hydrogen storage properties of novel Li-based hydrides for energy applications. *Int J Hydrogen Energy.* 2025;117:300–313.
- [4] Evro S, Tomomewo OS. Green hydrogen integration in distributed energy systems: A comprehensive techno-economic and policy analysis. *Int J Hydrogen Energy.* 2025;148:149895.
- [5] Hamid A, Deris RRR, Shaffee SNA, Hin TYY, Ametefe DS, Ibrahim ML. A systematic review on environmentally friendly hydrogen production methods: Comparative analysis of reactor technologies for optimal efficiency and sustainability. *Sustain Chem Clim Action.* 2025;100088.
- [6] Yamçıçier Ç, Al S, Kürkçü C. Theoretical investigations on structural, electronic, elastic, thermal, optic and hydrogen storage properties of $XAlH_6$ ($X = La, Ce, Pr$) aluminium hydrides. *Physica B: Condens Matter.* 2025;417713.
- [7] ur Rehman Z, Rehman MA, Rehman B, Amjad M, Awais M, Iqbal I, Rafique A. A DFT study of structural, electronic, mechanical, phonon, thermodynamic, and H_2 storage properties

of lead-free perovskite hydride MgXH_3 ($X = \text{Cr, Fe, Mn}$). *J Phys Chem Solids*. 2024;186:111801.

[8] Ayyaz A, Alkhaldi HD, Saidi S, Albalawi H, Zayed O, Al-Daraghme TM, et al. DFT investigation of thermodynamic, electronic, optical, and mechanical properties of XLiH_3 ($X = \text{Mg, Ca, Sr, Ba}$) hydrides for hydrogen storage and energy harvesting. *Mater Sci Semicond Process*. 2025;186:109020.

[9] Raza HH, Naeem M, Ali HS, Parveen A, Al-Enizi AM. First-principles investigation of BX_3H_9 ($X = \text{Ca, Sc, Ti}$) hydrides: Structural, electronic, phonon, and hydrogen storage properties. *J Phys Chem Solids*. 2025;112800.

[10] Ishaq H, Dincer I, Crawford C. A review on hydrogen production and utilization: Challenges and opportunities. *Int J Hydrogen Energy*. 2022;47(62):26238–26264.

[11] Surucu G, Candan A, Gencer A, Isik M. First-principle investigation for the hydrogen storage properties of NaXH_3 ($X = \text{Mn, Fe, Co}$) perovskite type hydrides. *Int J Hydrogen Energy*. 2019;44(57):30218–30225.

[12] Tang T, Tang Y. First-principles investigations for the structural, optoelectronic and hydrogen storage properties of double perovskite $\text{KNaMg}_2\text{F}_{6-x}\text{H}_x$ and KNaAe_2H_6 ($\text{Ae} = \text{Be, Mg, Ca}$). *Int J Hydrogen Energy*. 2024;61:13–24.

[13] Wang J, Azam W. Natural resource scarcity, fossil fuel energy consumption, and total greenhouse gas emissions in top emitting countries. *Geosci Front*. 2024;15(2):101757.

[14] Hosen, A., Mousa, A. A., Nemati-Kande, E., Khan, A. N., Abu-Jafar, M. S., Benassi, E., & Asad, J. (2025). *Systematic computational screening and design of double perovskites $Q_2\text{LiMH}_6$ ($Q = \text{K, Rb}$; $M = \text{Ga, In, Tl}$) for efficient hydrogen storage: A DFT and AIMD approach. *Surfaces and Interfaces*, 106608.*

[15] Touti, R., El Mekkaouy, A., Didi, Y., Tahiri, A., & Chtita, S. (2025). *Computational analysis of $X_2\text{MgTiH}_6$ ($X = \text{Li, Na, and K}$) double perovskite hydride materials for hydrogen storage applications. *International Journal of Hydrogen Energy*, 161, 150644.*

- [16] Rehman, M. A., Rehman, Z. U., Usman, M., Alomar, S. Y., Khan, M. J., & Fatima, J. (2024). *Exploring the hydrogen storage in novel perovskite hydrides: A DFT study*. *International Journal of Hydrogen Energy*, 84, 447–456.
- [17] Al-Zoubi, N., Almahmoud, A., Almahmoud, A., & Obeidat, A. (2024). *Theoretical assessment of novel NaXH_3 and KXH_3 ($X = \text{Tc, Ru, and Rh}$) perovskite hydrides for hydrogen storage*. *International Journal of Hydrogen Energy*, 93, 822–831.
- [18] Obeidat, A., Almahmoud, A., Alkhalidi, H., & Gharaibeh, M. (2025). *First-principles examination of the structural, hydrogen storage, mechanical, electronic, and optical properties of $\text{K}_2\text{Ba}_{1-x}\text{Ga}_x\text{H}_6$ ($B = \text{Li, Na; } x = 0, 0.25, 0.5, 0.75, 1$) double perovskite hydrides*. *International Journal of Hydrogen Energy*, 153, 150286.
- [19] Ahmed, B., Tahir, M. B., Sagir, M., Parveen, A., Abbas, Z., & Nassani, A. A. (2025). *First-principles study of Ti-based X_2TiH_5 ($X = \text{Mg, Ca, Sr}$) hydrides for advanced hydrogen storage applications*. *Chemical Physics*, 589, 112499.
- [20] Berri S, Yamçıçier Ç. First-principles analysis to evaluate the crystal stability, hydrogen storage, mechanical behavior and electronic structure of $\text{Mg}_7\text{XH}_{16}$ ($X = \text{Ti, Mn, Fe}$). *Int J Hydrogen Energy*. 2025;177:151559.
- [21] Ahmed B, Tahir MB, Sagir M, Parveen A, Abbas Z, Al-Aiban KM. Unveiling the potential of XInH_3 ($X = \text{Rb, Cs}$): A DFT study for solid-state hydrogen storage applications. *J Chem Phys*. 2025;588:112441.
- [22] Ahmed B, Tahir MB, Ali A, Sagir M. DFT insights on structural, electronic, optical and mechanical properties of double perovskites X_2FeH_6 ($X = \text{Ca, Sr}$) for hydrogen-storage applications. *Int J Hydrogen Energy*. 2024;50:316–324.
- [23] Siddique A, Khalil A, Almutairi BS, Tahir MB, Sagir M, Ullah Z, et al. Structures and hydrogen storage properties of AeVH_3 ($\text{Ae} = \text{Be, Mg, Ca, Sr}$) perovskite hydrides by DFT calculations. *Int J Hydrogen Energy*. 2023;48:24401.
- [24] Archi M, Bajjou O, Elhadadi B. A comparative ab initio analysis of the stability, electronic, thermodynamic, mechanical, and hydrogen storage properties of SrZnH_3 and SrLiH_3

perovskite hydrides through DFT and AIMD approaches. *Int J Hydrogen Energy*. 2025;105:759–770.

[25] Bahhar S, Tahiri A, Jabar A, Louzazni M, Idiri M, Bioud H. DFT-based first-principles calculations of new NaXH_3 ($X = \text{Ti, Cu}$) hydride compounds for hydrogen storage applications. *Comput Mater Sci*. 2024;238:112928.

[26] Mubashir M, Ali M, Yousaf M, Huang H, Khan MJ. Exploring promising KAH_3 ($A = \text{Ca, Sr, Ba}$) hydrides for solid-state hydrogen storage and thermoelectric applications. *Int J Hydrogen Energy*. 2024;82:1435–1445.

[27] Ez-Zahraouy H. Enhancing hydrogen storage properties of titanium hydride TiH_2 with vacancy defects and uniaxial strain: A first-principles study. *Int J Hydrogen Energy*. 2024;87:678–85.

[28] Azavi B, Javvaji B, Shojaei F, Rabczuk T, Shapeev AV, Zhuang X. Exceptional piezoelectricity, high thermal conductivity and stiffness, and promising photocatalysis in two-dimensional MoSi_2N_4 family confirmed by first-principles. *Nano Energy*. 2021;82:105716.

[29] Mortazavi B, Podryabinkin EV, Novikov IS, Rabczuk T, Zhuang X, Shapeev AV. Accelerating first-principles estimation of thermal conductivity by machine learning interatomic potentials: A MTP/ShengBTE solution. *Comput Phys Commun*. 2021;258:107583.

[30] Ahmed B, Tahir MB, Khan N, Parveen A, Abbas Z, Sagir M, Dahshan A. Hydrogen storage potential of XNiH_3 ($X = \text{Sr, Ba}$) compounds: A comprehensive DFT analysis. *Phys Lett A*. 2024;525:129899.

[31] Fischer TH, Almlof J. General methods for geometry and wave function optimization. *J Phys Chem*. 1992;96(24):9768–9774.

[32] Hosen A, Dahliah D, Mohammad NFA, Mousa AA, Abu-Jafar MS. A computational study on the comparative analysis of tetragonal complex metal hydride Q_2FeH_5 ($Q = \text{Mg, Ca, Sr}$) for hydrogen storage applications. *Int J Hydrogen Energy*. 2025;102:348–359.

- [33] Du Y, Xu N, Chen S, Chen Y, Song R, Luo W, Zhang W. First-principles study of the hydrogen storage properties of hydride perovskites XCuH_3 ($\text{X} = \text{K}, \text{Rb}$) for hydrogen storage applications. *Int J Hydrogen Energy*. 2024;78:713–720.
- [34] Ehrenreich H. Band structure and transport properties of some 3–5 compounds. *J Appl Phys*. 1961;32(10):2155–2166.
- [35] Mera A, Rehman MA. First-principles investigation for the hydrogen storage properties of AeSiH_3 ($\text{Ae} = \text{Li}, \text{K}, \text{Na}, \text{Mg}$) perovskite-type hydrides. *Int J Hydrogen Energy*. 2024;50:1435–1447.
- [36] Yiğit T, Öztürk H, Yamçıçier Ç. X_2AlH_7 ($\text{X} = \text{Ca}, \text{Sr}, \text{Ba}$) hydrides as next-generation hydrogen storage materials: A comprehensive first-principles study on structural, mechanical, optical, electronic and thermophysical properties. *J Energy Storage*. 2025;129:117400.
- [37] Zaman M, Ayyaz A, Ashraf S, Aljameel AI, Alkhaldi HD, Binzowaimil AM, et al. Revealing hydrogen storage, thermodynamic, electronic, and mechanical aspects of perovskite hydrides GaXH_3 ($\text{X} = \text{Si}, \text{Ge}$): First-principles approach. *Energy*. 2025;138578.
- [38] Liu D, Dai X, Cai Y, Cao K, Liu F, Zeng H, Sa R. First-principles comparative analysis of structural stability, hydrogen storage, mechanical, and electronic properties of hexahydride perovskites $\text{A}_2(\text{Pd/Pt})\text{H}_6$ ($\text{A} = \text{alkali metal}$). *Mater Des*. 2025;114660.
- [39] Masood M, Murtaza G, Ahmad N, Touqir M, Hafiz I, Usman A, et al. Ab initio study of the physical properties of Ge-based perovskites (XGeH_3 : $\text{X} = \text{Mg}, \text{Ca}, \text{Sr}$) for potential hydrogen storage application. *Int J Hydrogen Energy*. 2025;97:981–993.
- [40] Bahhar S, Tahiri A, Jabar A, Louzazni M, Idiri M, Bioud H. Computational assessment of MgXH_3 ($\text{X} = \text{Al}, \text{Sc}, \text{Zr}$) hydrides materials for hydrogen storage applications. *Int J Hydrogen Energy*. 2024;58:259–267.
- [41] Pokluda J, Černý M, Šob M, Umeno Y. Ab initio calculations of mechanical properties: Methods and applications. *Prog Mater Sci*. 2015;73:127–158.

- [42] Archi M, Bajjou O, Elhadadi B. Theoretical DFT insights into the stability, electronic, mechanical, optical, thermodynamic, and hydrogen storage properties of RbXH_3 ($X = \text{Si, Ge, Sn}$) perovskite hydrides. *Mater Res Bull.* 2025;188:113434.
- [43] Gaillac R, Pullumbi P, Coudert FX. ELATE: An open-source online application for analysis and visualization of elastic tensors. *J Phys Condens Matter.* 2016;28(27):275201.
- [44] El Fatouaki Z, Tahiri A, Jabar A, Idiri M. Designing Mn_3NaH_8 and Mn_3KH_8 hydride perovskites for efficient hydrogen storage via density functional theory. *Int J Hydrogen Energy.* 2025;175:151433.
- [45] El Fatouaki Z, Jabar A, Tahiri A, Idiri M. Study by DFT and AIMD: Structural, mechanic, electronic and thermodynamic properties of AZrF_6 for solid electrolyte applications. *Solid State Commun.* 2025;116155.
- [46] Barron THK, White GK. Heat Capacity and Thermal Expansion at Low Temperatures. 2nd ed. Springer Science & Business Media; 2012.
- [47] Lei X, Yang A, Zhou L, Duan Y, Ma L, Li M, et al. First-principles calculations of phase stability, electronic structure, mechanical properties and thermal conductivities of TMH_2 ($\text{TM} = \text{V, Nb, Ta}$) metal hydrides. *Mater Today Commun.* 2024;41:110549.
- [48] El Fatouaki Z, Tahiri A, Jabar A, Idiri M. First-principles study on the physical properties of double perovskites LiX_3H_8 ($X = \text{Ni, Mn}$) for hydrogen storage. *J Phys Chem Solids.* 2025;112867.
- [49] Rahman MA, Hossain AA. Investigating the physical and hydrogen storage properties of alkali metal-based cobalt hydrides. *Int J Hydrogen Energy.* 2025;97:457–468.
- [50] Yamçıçılar Ç, Kürkçü C. Structural, elastic, optic, electronic, phonon, thermodynamic, and hydrogen storage properties of bialkali alanates M_2LiAlH_6 ($M = \text{Na, K}$). *Int J Hydrogen Energy.* 2025;135:440–456.
- [51] Zhang J, Chen S, Hou J, Chen Y, Liu J, Xu N, et al. First-principles study of mechanical, electronic structure, optical, thermodynamic properties and hydrogen storage for new hydride perovskites XInH_3 ($X = \text{Rb, Cs}$). *Physica B Condens Matter.* 2024;695:416488.

- [52] Masood MK, Chaoui K, Khan W, Bahajjaj AAA, Bibi S, Kanwal A, et al. Unveiling the potential platinum-based hydrides for solid-state hydrogen storage application: A DFT study. *Mater Sci Semicond Process*. 2025;188:109214.
- [53] Yamçıçier Ç, Kürkçü C. Investigation of structural, electronic, elastic, vibrational, thermodynamic, and optical properties of Mg_2NiH_4 and Mg_2RuH_4 compounds used in hydrogen storage. *J Energy Storage*. 2024;84:110883.
- [54] Zhu Y, Liang Y, Pu Y, Xiong J. Investigation for the hydrogen storage properties of XCrH_3 ($\text{X} = \text{Na}, \text{K}$) and KYH_3 ($\text{Y} = \text{Mo}, \text{W}$) perovskite type hydrides based on first-principles. *Int J Hydrogen Energy*. 2024;71:239–249.
- [55] Feher A, Kotlar A, Manzhelii E, Syrkin E, Gospodarev I, Kravchenko K, et al. The features of low frequency atomic vibrations and propagation of acoustic waves in heterogeneous systems. In: *IntechOpen*; 2011.
- [56] Song X, Zhao Y, Ni J, Meng S, Dai Z. Strong anharmonic phonon scattering and superior thermoelectric properties of Li_2NaBi . *Mater Today Phys*. 2023;31:100990.
- [57] El Fatouaki Z, Tahiri A, Jabar A, Idiri M. Novel alkali metal AFe_3H_8 ($\text{A} = \text{Na}, \text{K}, \text{Rb}$) hydrides explored by first-principles calculations for hydrogen storage. *Int J Hydrogen Energy*. 2025;183:151849.
- [58] Chen LQ. *Thermodynamic Equilibrium and Stability of Materials*. Singapore: Springer; 2022.
- [59] Rafique A, Usman M, Rehman JU, Nazeer A, Ullah H, Hussain A. Investigation of structural, electronic, mechanical, optical and hydrogen storage properties of cobalt-based hydride-perovskites XCoH_3 ($\text{X} = \text{In}, \text{Mn}, \text{Sr}, \text{Sn}, \text{Cd}$) for hydrogen storage application. *J Phys Chem Solids*. 2023;181:111559.